

Unsupervised full-field Bayesian inference of orthotropic hyperelasticity from a single biaxial test: a myocardial case study

Rogier P. Krijnen^a, Akshay Joshi^b, Siddhant Kumar^c, Mathias Peirlinck^{a,*}

^a*Dept. of BioMechanical Engineering, Delft University of Technology, Netherlands,*

^b*Dept. of Mechanical Engineering, Indian Institute of Science, Bengaluru, India,*

^c*Dept. of Materials Science and Engineering, Delft University of Technology, Netherlands,*

Abstract

Cardiac muscle tissue exhibits highly non-linear hyperelastic and orthotropic material behavior during passive deformation. Traditional constitutive identification protocols therefore combine multiple loading modes and typically require multiple specimens and substantial handling. In soft living tissues, such protocols are challenged by inter- and intra-sample variability and by manipulation-induced alterations of mechanical response, which can bias inverse calibration. In this work we exploit spatially heterogeneous full-field kinematics as an information-rich alternative to multimodal testing. We adapt EUCLID, an unsupervised method for the automated discovery of constitutive models, towards Bayesian parameter inference for highly nonlinear, orthotropic constitutive models. Using synthetic myocardial tissue slabs, we demonstrate that a single heterogeneous biaxial experiment, combined with sparse reaction-force measurements, enables robust recovery of Holzapfel–Ogden parameters with quantified uncertainty, across multiple noise levels. The inferred responses agree closely with ground-truth simulations and yield credible intervals that reflect the impact of measurement noise on orthotropic material model inference. Our work supports single-shot, uncertainty-aware characterization of nonlinear orthotropic material models from a single biaxial test, reducing sample demand and experimental manipulation.

Keywords: material model inference, full-field kinematics, uncertainty quantification, anisotropic hyperelasticity, experimental tissue testing, Bayesian inference

1. Introduction

Soft biological tissues exhibit complex mechanical responses due to their fibrous, anisotropic microstructure. Accurately characterizing this behavior is essential for constructing predictive constitutive models that support simulation-driven design, diagnostics, and treatment planning [1, 2]. However, unlike engineered materials, soft tissues are subject to considerable biological variability, both within a patient, across a patient cohort, and across experimental studies [3, 4, 5, 6, 7]. This intra- and inter-sample variability is even more pronounced in the myocardium, where strong spatial gradients in myofiber orientation and laminar architecture govern regional mechanical function [8, 9]. Here, we investigate the impact that the underlying microstructural organization variability has on the mechanical behavior of a single sample.

Traditional approaches to constitutive modeling of such tissues typically rely on multiple mechanical tests across different deformation modes including uniaxial tension or compression, biaxial tension, or shear testing [10, 11, 12]. These protocols often require combining data from different specimens and, as such, ignore and smooth out intrinsic

*Correspondence:

Email address: `mplab-me@tudelft.nl` (Mathias Peirlinck)

intra- and inter-sample variability into an average response [13]. Moreover, these protocols involve strong assumptions, such as spatially homogeneous stress and strain fields within the region of interest [14, 15, 16]. Such assumptions are problematic for living tissues, where spatial heterogeneity is the norm, and the mechanical response may depend on subtle differences in fiber orientation, geometry, or mounting. In addition, invasive sample manipulations, such as cutting, clamping, and gluing, can alter the intrinsic mechanical behavior that these tests seek to measure [17, 18, 19].

These challenges have prompted the development of single-sample, single-experiment methodologies that aim to infer full constitutive behavior from a single loading protocol. This shift has been enabled by advances in full-field deformation measurements, such as digital image correlation and imaging-based 3D kinematics [20, 21, 22]. When applied to samples undergoing spatially heterogeneous deformation, such data enable the inference of multiple material parameters simultaneously, reducing the need for multiple loading modes. Indeed, unsupervised identification techniques, such as the virtual fields method (VFM) [23, 24], finite element model updating (FEMU) [25, 26, 27], variational systems identification [20], the equilibrium gap method (EGM) [28, 29], and EUCLID [30, 31, 32, 33], demonstrate that heterogeneous strain states, once seen as a nuisance, can be leveraged as rich sources of information, obviating the need for homogenizing assumptions. In this study, we assess the extent to which a simple biaxial tensile testing protocol on a single myocardial tissue slab can support identification of the underlying orthotropic behavior.

Yet, a key limitation persists in most current workflows: the lack of uncertainty quantification. Material parameters are frequently reported as point estimates, with little accounting for the inherent measurement noise or biological variability. In the context of myocardial modeling, where even adjacent samples can differ markedly in stiffness and fiber orientation [10, 34], such deterministic inference may be misleading [35]. Recent work has begun to address this gap through Bayesian approaches to inverse modeling, which offer not only best-fit estimates but also posterior distributions reflecting uncertainty in data and model form [36, 32, 37, 38, 39, 40, 41]. Within the unsupervised setting, Bayesian-EUCLID forms an interesting contribution towards the inference of myocardial tissue behavior from full-field displacement fields and force measurements. In prior work, Joshi et al. demonstrated the feasibility of using Gibbs sampling for full-field inference in two-dimensional problems [32], where the material response could be inferred from a linear system of equations for the unknown material parameters in a rich constitutive feature library.

In contrast, the setting of this study involves two distinct and compounding challenges. First, the underlying constitutive models are highly nonlinear [42, 14, 16], with strongly cross-correlated parameters [15, 43] that give rise to complex posterior landscapes. Second, we transition to three-dimensional full-field data. While the latter provides richer information, it also substantially increases the computational cost of evaluating the likelihood function. These factors independently and jointly limit the practical utility of Markov Chain Monte Carlo (MCMC) methods, including Gibbs sampling, due to the high cost of repeated likelihood evaluations and the poor mixing behavior in high-dimensional, correlated spaces. These limitations motivates adapting the Bayesian EUCLID framework with more scalable inference strategies, such as Stochastic Variational Inference (SVI), which approximates posterior distributions through optimization rather than sampling, enabling tractable inference in settings with both complex models and large data volumes.

Towards these goals, this study presents an unsupervised, full-field, Bayesian framework for the inference of orthotropic hyperelastic material parameters from a single heterogeneous biaxial tensile test. Our approach builds on the Bayesian-EUCLID framework [32], extended via SVI to capture parametric uncertainty in a highly nonlinear, a priori chosen constitutive model form. The myocardium is modeled using the well-established Holzapfel–Ogden constitutive law [14, 44], and heterogeneity in the deformation field is introduced either through microstructural variation (i.e., intrinsic fiber-sheet-interlaminar architectural heterogeneity), geometric tissue sample modification, or both. We demonstrate that the spatial richness of the heterogeneous displacement field combined with reaction force data enables robust parameter inference with uncertainty quantification from a single test. We additionally validate the inferred material models using unseen invariant values and assess sensitivity to displacement noise. Overall, this work highlights the potential of full-field, unsupervised, and uncertainty-aware approaches to redefine how we efficiently characterize complex biological tissues, taking into account minimal tissue availability and minimizing tissue manipulation.

2. Unsupervised Stochastic Variational constitutive parameter inference

Conventional approaches for characterizing myocardial material behavior typically rely on spatially averaged measurements and simplifying assumptions of spatially homogeneous microstructural organization. However, this intrinsic homogenization obscures the spatial heterogeneity present within a tissue sample. To address this, we infer the constitutive parameter vector in an unsupervised setting from experimentally accessible data: (i) global reaction forces, (ii) full-field deformation, and (iii) microstructural organization across the slab. In this work, we assume digital volume correlation (DVC) data derived from concomitant through-thickness imaging, such as ultrasound [45], Magnetic Resonance Imaging [46], or X-Ray Imaging [47] to obtain three-dimensional deformation fields. In parallel, microstructural maps can be obtained via SHG or micro-CT [48, 12, 49]. Among established inverse constitutive identification strategies such as FEMU, VFM, and EGM, we build on EUCLID [30]. EUCLID formulates the inverse problem via the weak form of momentum balance (see Section 2.1). Here, we adapt it to a fully three-dimensional setting with nonlinear orthotropic materials and recast the classic deterministic parameter optimization into an unsupervised Bayesian inference problem. Leveraging Stochastic Variational Inference (SVI), we identify orthotropic hyperelastic parameters from a single biaxial test; the overall workflow is summarized in Figure 1 and detailed in Section 2.2.

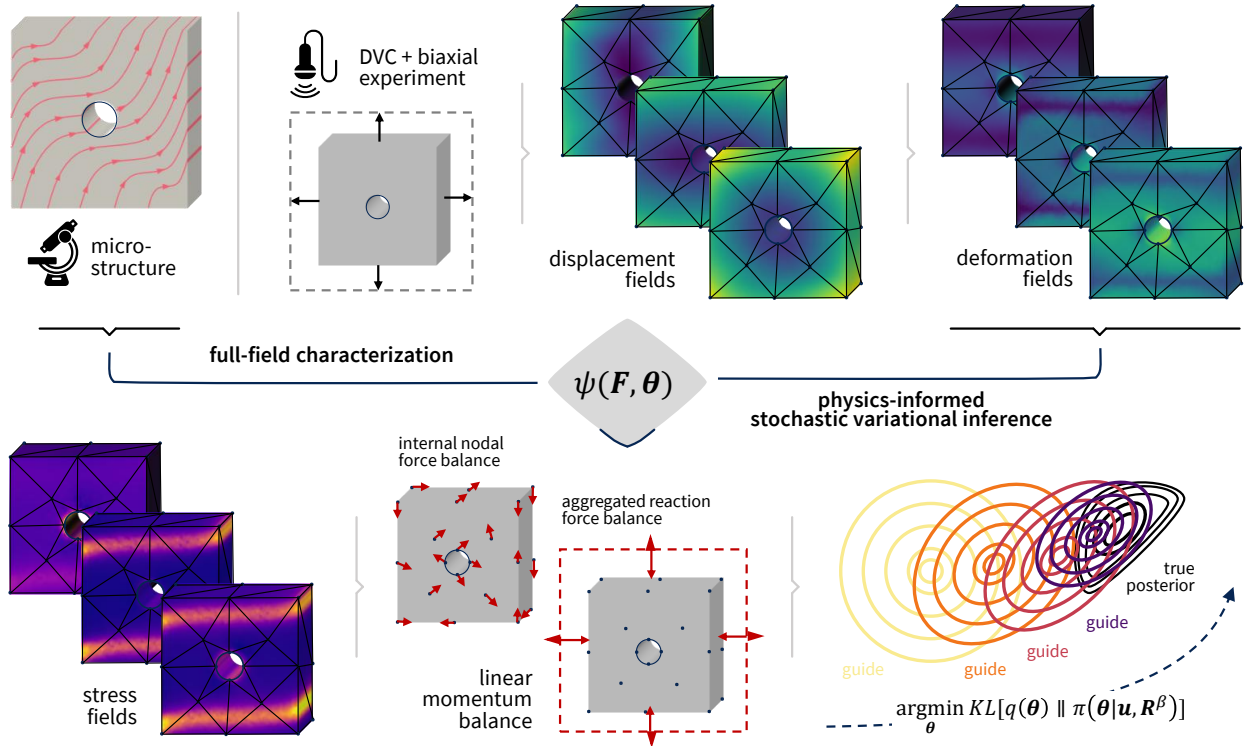


Figure 1: **Schematic overview of our unsupervised full-field stochastic variational inference framework for orthotropic hyperelastic tissue behavior.** Quantification of the tissue’s microstructural organization, such as spatially varying fiber orientations, provides essential architectural information across the sample domain. In parallel, point-wise measurements of displacements \mathbf{u} and reaction forces \mathbf{R}^β are acquired under quasi-static biaxial loading using digital volume correlation. The sample geometry is discretized into a finite element mesh, enabling reconstruction of continuous deformation fields \mathbf{F} from the measured data. A nonlinear orthotropic constitutive model ψ , parameterized by a set of cross correlated material parameters θ , serves as the mechanistic basis for inference. Given the reconstructed deformation and microstructural organization fields, the model predicts stress responses at the element level, which are used to compute internal and external nodal forces. Residuals are formulated through the weak form of the conservation of linear momentum, minimized pointwise for unconstrained degrees of freedom and in aggregate at boundaries with known reaction forces. The inverse problem is cast as a stochastic variational inference task, where a variational guide distribution $q(\theta)$ approximates the true posterior $\pi(\theta | \mathbf{u}, \mathbf{R}^\beta)$ by minimizing the Kullback-Leibler divergence $\text{KL}(q(\theta) || \pi(\theta | \mathbf{u}, \mathbf{R}^\beta))$. Our physics-informed constitutive inference framework enables efficient and scalable inference from complex high dimensional full-field deformation datasets, accommodating nonlinear material behaviors and cross-correlated parameter effects.

2.1. EUCLID preliminaries

We first define the kinematic and force data available from a single experiment, and then derive the equilibrium residuals that underpin deterministic parameter identification. Consider a myocardial tissue specimen undergoing quasi-static deformation in a three-dimensional reference domain $\Omega \subset \mathbb{R}^3$. Depending on the tissue slab's extraction orientation protocol (see Section 3), the underlying myocardial microstructure variation induces diverse and heterogeneous strain states. In this work, this heterogeneity enters through spatially varying structural fields, while the constitutive parameter vector θ is assumed to be spatially homogeneous and thus constant over Ω . This separation attributes spatial variability to the structural inputs while keeping the inverse problem focused on a single parameter vector. Optionally, additional tissue manipulations, e.g., cutting a hole in the tissue slab or local cardiac ablation, can further promote a highly heterogeneous deformation state during biaxial tensile testing.

Boundary conditions are applied such that Dirichlet conditions are enforced on $\partial\Omega_u \subset \partial\Omega$ and Neumann conditions on the remainder, $\partial\Omega_t = \partial\Omega \setminus \partial\Omega_u$. For simplicity, our analysis focuses on displacement-controlled loading (i.e., Dirichlet boundary conditions), while noting that applied forces in load-controlled scenarios are equivalent to reaction forces under displacement control. The dataset comprises n_t snapshots of displacement measurements,

$$\{\mathbf{u}^{a,t} \in \mathbb{R}^3 : a = 1, \dots, n_n; t = 1, \dots, n_t\}, \quad (1)$$

recorded at n_n reference points comprising the measurement node set:

$$\{\mathbf{X}^a \in \Omega : a = 1, \dots, n_n\}. \quad (2)$$

Additionally, for each snapshot, n_β reaction forces

$$\{\mathbf{R}^{\beta,t} \in \mathbb{R}^3 : \beta = 1, \dots, n_\beta; t = 1, \dots, n_t\} \quad (3)$$

are measured at selected Dirichlet boundaries (e.g., using load cells). Since $n_\beta \ll n_n$, the reaction force data are sparse compared to the dense displacement field. For brevity, the superscript $(\cdot)^t$ is omitted in the subsequent discussion, although the numerical procedure is applied independently to every snapshot. Given $\{\mathbf{u}^a\}$ and $\{\mathbf{R}^\beta\}$, our goal is to infer the parameter set θ of an a priori assumed constitutive model $\psi(\mathbf{F}, \theta)$.

To connect the measurements to equilibrium, we first reconstruct a continuous kinematic field and its deformation gradient. The reference domain Ω is discretized using linear tetrahedral elements, evaluated with a single quadrature point at its barycenter, yielding

$$\mathbf{u}(\mathbf{X}) = \sum_{a=1}^{n_n} N^a(\mathbf{X}) \mathbf{u}^a. \quad (4)$$

Here, $N^a : \Omega \rightarrow \mathbb{R}$ represents the shape function associated with the measurement node \mathbf{X}^a . We subsequently approximate the corresponding deformation gradient field as

$$\mathbf{F}(\mathbf{X}) = \mathbf{I} + \sum_{a=1}^{n_n} \mathbf{u}^a \otimes \nabla N^a(\mathbf{X}), \quad (5)$$

where \mathbf{I} is the identity matrix, and ∇ represents the gradient operator with respect to the reference coordinates \mathbf{X} .

Assuming hyperelasticity, i.e., no dissipative energy losses within the material, the first Piola Kirchhoff stress follows as

$$\mathbf{P}(\mathbf{F}) = \frac{\partial \psi(\mathbf{F}, \theta)}{\partial \mathbf{F}} \quad (6)$$

as the constitutive relation between the first Piola Kirchhoff stress \mathbf{P} and the deformation gradient \mathbf{F} defined through the free energy function ψ and parameterized using the constitutive parameter set θ [50, 51, 52]. In particular, \mathbf{P} depends on the unknown parameters through $\psi(\mathbf{F}, \theta)$.

We leverage the conservation of linear momentum to guide the learning of the constitutive model parameter set, which eliminates the need for stress labels [30, 31]. Assuming quasi-static loading conditions and negligible body forces, the weak form of the linear momentum balance in our reference domain Ω is given by

$$\int_{\Omega} \mathbf{P}(\mathbf{F}, \boldsymbol{\theta}) : \nabla \mathbf{v} \, dV - \int_{\partial\Omega_t} \bar{\mathbf{t}} \cdot \mathbf{v} \, dS = 0 \quad \forall \text{ admissible } \mathbf{v}, \quad (7)$$

where $\bar{\mathbf{t}}$ denotes the prescribed traction acting on $\partial\Omega_t$, per unit reference area and \mathbf{v} is a test function that is sufficiently regular and vanishes on the Dirichlet boundary $\partial\Omega_u$. We prefer the weak formulation over the strong form, as it avoids the need for second order derivatives with respect to the displacement field, which are sensitive to measurement noise. In our displacement-controlled setting, non-instrumented free surfaces are typically traction free (so $\bar{\mathbf{t}} = 0$ there). Measured boundary forces enter through reactions on $\partial\Omega_u$, which we incorporate below.

Let $\mathcal{D} = \{(a, i) : a = 1, \dots, n_n; i = 1, 2, 3\}$ denote all the displacement degrees of freedom in our domain Ω , which we partition into $\mathcal{D}^{\text{free}}$, the unconstrained degrees of freedom, and $\mathcal{D}_{\beta}^{\text{fix}}$ (with $\beta = 1, \dots, n_{\beta}$) denoting the degrees of freedom under Dirichlet constraints that contribute to the observed reaction force R^{β} . Using a Bubnov–Galerkin discretization, we approximate the admissible test function \mathbf{v} as

$$\mathbf{v}(\mathbf{X}) = \sum_{a=1}^{n_n} N^a(\mathbf{X}) \mathbf{v}^a, \quad \text{with } v_i^a = 0 \quad \forall (a, i) \in \bigcup_{\beta=1}^{n_{\beta}} \mathcal{D}_{\beta}^{\text{fix}}, \quad (8)$$

and introducing our constitutive relation (6), our weak form (7) reduces to

$$\sum_{a=1}^{n_n} v_i^a f_i^a = 0, \quad \text{with } f_i^a = \underbrace{\int_{\Omega} P_{ij} \nabla_j N^a \, dV}_{\text{internal force}} - \underbrace{\int_{\partial\Omega_t} \bar{t}_i N^a \, dS}_{\text{external force}}. \quad (9)$$

The integrals are evaluated by numerical quadrature on the same discretization as (4). Since the test functions are arbitrary on $\mathcal{D}^{\text{free}}$, the force residual must vanish at every unconstrained degree of freedom,

$$f_i^a = 0 \quad \forall (a, i) \in \mathcal{D}^{\text{free}}. \quad (10)$$

At the fixed degrees of freedom, the internal and external forces are counteracted by the reaction force imposed by the Dirichlet constraints. Because point-wise reactions are not accessible experimentally, we treat them as unavailable. Instead, we use the measured reaction forces integrated over instrumented boundary segments, which yields the global balance constraint

$$\sum_{(a,i) \in \mathcal{D}_{\beta}^{\text{fix}}} f_i^a = R^{\beta} \quad \forall \quad \beta = 1, \dots, n_{\beta}, \quad (11)$$

where the summation is carried out over all point-wise forces associated with the degrees of freedom in the β^{th} Dirichlet constraint, denoted as $\mathcal{D}_{\beta}^{\text{fix}}$.

Together, (10) and (11) constitute a system of equations that defines the inverse problem of constitutive model inference [30, 31, 33]. We deterministically solve for $\boldsymbol{\theta}^*$ by minimizing the equilibrium residuals over all snapshots:

$$\boldsymbol{\theta}^* \leftarrow \arg \min_{\boldsymbol{\theta}} \sum_{t=1}^{n_t} \left[\underbrace{\sum_{(a,i) \in \mathcal{D}^{\text{free}}} (f_i^{a,t})^2}_{\text{free degrees of freedom}} + \sum_{\beta=1}^{n_{\beta}} \underbrace{\left(R^{\beta,t} - \sum_{(a,i) \in \mathcal{D}_{\beta}^{\text{fix}}} f_i^{a,t} \right)^2}_{\text{fixed degrees of freedom}} \right], \quad (12)$$

such that the displacement and reaction force data satisfy the physics-based constraints (10) and (11).

2.2. Stochastic variational inference

In this study, we assume an a priori known constitutive law (28) and aim to infer the underlying constitutive parameter set θ together with its uncertainty. Leveraging Bayes' theorem, we combine prior beliefs about θ with a likelihood model that accounts for the impact of measurement noise on the physics-based residual constraints conditioned on the displacement and reaction force data.

We recast the deterministic optimization problem in (12) into Bayesian inference by treating the equilibrium residuals as the result of additive measurement noise. For a given snapshot $t = 1, \dots, n_t$, we define the residual vector

$$\boldsymbol{\rho}^t(\boldsymbol{\theta}) = \begin{bmatrix} \{f_i^{a,t}\}_{(a,i) \in \mathcal{D}^{\text{free}}} \\ \left\{ R^{\beta,t} - \sum_{(a,i) \in \mathcal{D}_\beta^{\text{fix}}} f_i^{a,t} \right\}_{\beta=1}^{n_\beta} \end{bmatrix}, \quad (13)$$

and stack all snapshots into a single global residual

$$\boldsymbol{\rho}(\boldsymbol{\theta}) = \begin{bmatrix} \boldsymbol{\rho}^1(\boldsymbol{\theta}) \\ \vdots \\ \boldsymbol{\rho}^{n_t}(\boldsymbol{\theta}) \end{bmatrix} \quad (14)$$

This construction removes the need to carry superscript $(\cdot)^t$ in the subsequent probabilistic expressions while still retaining the multi-snapshot information. Note that $\boldsymbol{\rho}(\boldsymbol{\theta})$ implicitly depends on observed displacements and reaction forces through the constitutive response leading to the predicted forces in f_i^a .

We assume that the stacked residuals follow a multivariate normal distribution with zero mean and isotropic variance, reflecting the assumption of additive Gaussian noise:

$$\boldsymbol{\rho}(\boldsymbol{\theta}) \sim \mathcal{N}(\mathbf{0}, \sigma^2 \mathbf{I}) \quad (15)$$

which yields the likelihood

$$\pi(\mathbf{u}, R^\beta \mid \boldsymbol{\theta}, \sigma^2) \propto \exp\left(-\frac{1}{2\sigma^2} \|\boldsymbol{\rho}(\boldsymbol{\theta})\|^2\right) \quad (16)$$

In our case, both displacement field and reaction force measurements are affected by sensor noise, and we treat σ^2 as an effective residual variance that captures this combined uncertainty. Given that displacement propagates in a nonlinear fashion to the force residuals, we expect the residual variance to be dominated by displacement noise.

Next, we place priors on the residual noise variance σ^2 and the parameter vector $\boldsymbol{\theta}$. Since the variance of the measurement noise σ^2 is unknown and must be inferred, we assign an inverse-gamma prior:

$$\sigma^2 \sim \text{IG}(\alpha_\sigma, \beta_\sigma) \quad (17)$$

Concomitantly, we enforce physical constraints on the parameters by requiring them to be positive and therefore enforce a truncated normal distribution for the prior (truncated on the left at zero). Here, we introduce a scaling hyperprior v_s to decouple the overall measurement residual noise variance σ^2 from the underlying parameter prior variance:

$$\boldsymbol{\theta} \sim \mathcal{N}_+(\mathbf{0}, v_s \sigma^2 \mathbf{I}) \quad (18)$$

We place an inverse-gamma hyperprior on v_s :

$$v_s \sim \text{IG}(\alpha_{v_s}, \beta_{v_s}) \quad (19)$$

The hierarchical structure [32, 53, 54] of our prior distributions is showcased in Figure 2.

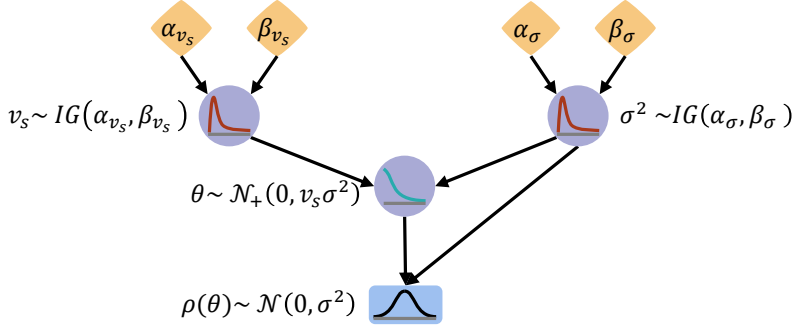


Figure 2: **Schematic of the hierarchical inference model.** This hierarchical Bayesian model places priors on both the residual variance in the likelihood and the constitutive model parameters. The red circular distributions represent hyperpriors for v_s and σ^2 , the light-blue circular distribution represents the prior on the material model parameters, and the black rectangular distribution represents the likelihood induced by the linear momentum balance residuals. The black arrows denote hierarchical dependencies. The hyperpriors are inverse-gamma distributed, the constitutive parameters are distributed according to a truncated multivariate normal distribution, and the likelihood is assumed to be normally distributed.

Combining the prior distributions (17)–(19) with the likelihood (16) yields the posterior:

$$\pi(\boldsymbol{\theta}, \sigma^2, v_s \mid \mathbf{u}, \mathbf{R}^\beta) \propto \pi(\mathbf{u}, \mathbf{R}^\beta \mid \boldsymbol{\theta}, \sigma^2) \pi(\boldsymbol{\theta} \mid \sigma^2, v_s) \pi(\sigma^2) \pi(v_s), \quad (20)$$

This posterior can, in principle, be approximated using *sampling-based* inference or *variational inference*. In simpler inference problems, sampling-based methods such as MCMC can often be relied on to approximate the posterior distribution. For example, Gibbs sampling has been successfully applied to two-dimensional full-field problems, where the material response could be inferred by solving a linear system of equations on a library of constitutive features [32]. In those cases, the constitutive models were potentially nonlinear in input but remained linear in their parameters, which keeps the posterior geometry relatively tractable for MCMC. In our setting, however, the constitutive models are nonlinear in both inputs and parameters, which induces strong parameter interactions and complex (often multi-modal) posteriors. Together with the cost of evaluating data-heavy 3D full-field likelihoods, this makes conventional MCMC-based posterior exploration computationally unattractive in practice.

We therefore adopt stochastic variational inference (SVI) to approximate the posterior efficiently using gradient-based optimization. SVI has been shown to substantially accelerate inference relative to MCMC in related settings [55, 53]. In SVI, we approximate the posterior distribution π with a tractable family of parametric guide distributions q . We employ a mean-field variational family q [56, 57], which assumes statistical independence between the quantities of interest,

$$q(\boldsymbol{\theta}, v_s, \sigma^2) = q(\boldsymbol{\theta}) q(\sigma^2) q(v_s) \quad (21)$$

with factors:

$$q(\boldsymbol{\theta}) = \mathcal{N}_+(\boldsymbol{\mu}^q, \boldsymbol{\Sigma}^q \circ \mathbf{I}) \quad (22)$$

$$q(\sigma^2) = \mathcal{IG}(\alpha_\sigma^q, \beta_\sigma^q) \quad (23)$$

$$q(v_s) = \mathcal{IG}(\alpha_{v_s}^q, \beta_{v_s}^q), \quad (24)$$

where \circ denotes the element-wise Hadamard product. The full set of variational parameters is denoted by $\Phi = \{\boldsymbol{\mu}^q, \boldsymbol{\Sigma}^q, \alpha_\sigma^q, \beta_\sigma^q, \alpha_{v_s}^q, \beta_{v_s}^q\}$, and hyperparameters are reported in Table 1. We specifically highlight $\boldsymbol{\mu}^q$, and $\boldsymbol{\Sigma}^q$ to be the location and scale parameters of the truncated normal distribution. These correspond to the mean and standard deviation of the underlying and untruncated normal distribution used in the definition of \mathcal{N}_+ .

To find the best approximation within this family, we minimize the Kullback-Leibler divergence [58, 59] between the

variational distribution q and the true posterior π , i.e.

$$\Phi^* \leftarrow \arg \min_{\Phi} \text{KL} \left(q_{\Phi} \left(\theta, v_s, \sigma^2 \right) \parallel \pi \left(\theta, v_s, \sigma^2 \mid \mathbf{u}, R^{\beta} \right) \right), \quad (25)$$

The entire inference pipeline is implemented in NumPyro [60], enabling automatic differentiation and stochastic optimization with ADAM using the reparameterization trick [61, 62]. Doing so, we alleviate the need to explicitly define the minimization procedure as was done in Thorat et al. [53]. We initialize the optimizer with a learning rate of $r_0 = 0.01$, and apply an exponential learning rate decay γ , i.e. $r_i = r_0 \gamma^{i/n_T}$ at epoch i with n_T denoting the total number of epochs.

Table 1: **Hyperparameters and simulation settings used in the stochastic variational inference framework and synthetic tissue slab data generation.** The upper rows list optimization settings and hierarchical Bayesian prior parameters used for the SVI guide distributions and model priors. The bottom rows summarize the geometry and loading conditions for the training and validation slab specimens, respectively.

Parameter	Notation	Value
<i>SVI hyperparameters:</i>		
weight for reaction force balance	λ_r	10
Optimizer	–	Adam
Number of epochs	n_T	100,000
Learning rate scheduler	–	exponential
Base learning rate	r_0	0.01
Learning decay rate	γ	0.1
<i>SVI guide hyperparameters:</i>		
Initial mean of \mathcal{N}_+ distribution	μ_{θ}	$10 + \epsilon^2 \times \{1, \dots, 1\}$, $\epsilon \sim \mathcal{N}(0, 1)$
Initial variance of \mathcal{N}_+ distribution	σ_{θ}^2	$10^{-18} \times \{1, \dots, 1\}$
Initial scale parameter for v_s	α_{v_s}	10^4
Initial rate parameter for v_s	β_{v_s}	10^4
Initial scale parameter for σ^2	a_{σ^2}	10^4
Initial rate parameter for σ^2	b_{σ^2}	10^4
<i>SVI model prior hyperparameters:</i>		
prior mean of \mathcal{N}_+ distribution	μ_{θ}	$10^{-10} \times \{1, \dots, 1\}$
prior variance of \mathcal{N}_+ distribution	σ_{θ}^2	$\{1, \dots, 1\}$
prior scale parameter for v_s	α_{v_s}	1
prior rate parameter for v_s	β_{v_s}	1
prior scale parameter for σ^2	α_{σ^2}	1
prior rate parameter for σ^2	β_{σ^2}	1
<i>Training slab specimen:</i>		
Number of nodes in mesh for FEM-based data generation	–	16, 856
Number of reaction force constraints	n_{β}	5
Number of data snapshots	n_t	2
Loading parameter	δ	$\{0.5 \times t : t = 2, 3\}$
Loading ratios	–	$\{(1 : 2), (1 : 1), (2 : 1)\}$
<i>Ground-truth material model parameters θ_{gt}:</i>		
Linear scaling parameters a_{\star} [kPa]	a, a_f, a_n, a_{f_s}	$\{0.809, 1.911, 0.227, 0.547\}$
Exponential scaling parameters b_{\star} [-]	b, b_f, b_n, b_{f_s}	$\{7.474, 22.063, 34.802, 5.691\}$
Bulk modulus [MPa]	K	0.1

3. Synthetic data generation

To assess our Bayesian inference framework under controlled conditions, we generate synthetic biaxial tensile testing data from high-resolution simulations of varying microstructurally and geometrically heterogeneous myocardial tissue slabs.

3.1. Myofiber architecture and tissue slab slicing

Informed by prior histological characterizations of myocardial tissue [8, 9, 14], we model our studied specimens as a layered orthotropic material in which cardiomyocytes align along main myofiber directions, packed by endomysial collagen into sheets, and connected via perimysial collagen. This organization defines three locally orthogonal directions: the fiber direction f , the sheet direction s , and the sheet-normal direction n . To investigate the role of heterogeneity in unsupervised constitutive parameter identifiability, we simulate myocardial tissue slabs that exhibit both *microstructure*-induced and *geometry*-induced heterogeneity.

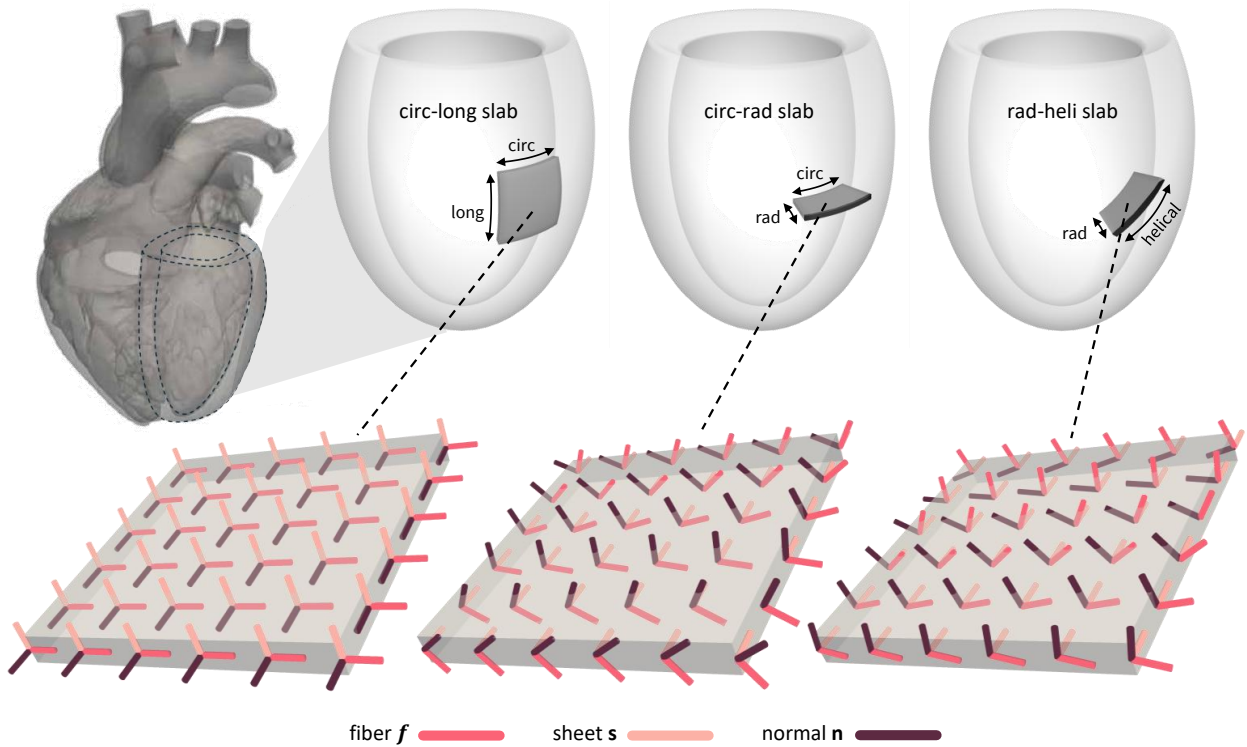


Figure 3: **Specimen slicing and microstructural organization.** Top: Schematic of the left ventricle and three considered slicing orientations to extract myocardial tissue slabs: circumferential–longitudinal (circ-long), circumferential–radial (circ-rad), and a rotated variant of the latter (rad-heli). Bottom: Each slicing orientation leads to a distinct microstructural configuration within the specimen. In circ-long slabs, the fiber direction lies in-plane and the sheet direction spans the through-thickness. Circ-rad slabs display a transmural fiber rotation from epicardium to endocardium, with the sheet direction aligned in the radial plane. The rad-heli orientation rotates the slab around the radial axis, aligning all three microstructural directions approximately within the plane of the specimen. Fiber directions (f) are shown in red, sheet directions (s) in pink, and normal directions (n) in brown.

Leveraging the intrinsic spatially varying myofiber architecture in the human heart [63], we extract three microstructurally distinct synthetic tissue slabs from the left ventricular free wall. All samples are assumed to be $10 \times 10 \times 1 \text{ mm}^3$ in size, representative of slabs from a healthy human left ventricular wall. The sample geometry and applied boundary conditions are summarized in [Appendix A](#).

Figure 3 showcases the microstructural variability across the slab domain, with directional fiber f , sheet s and normal n vectors discretized element-wise, and their spatial distribution depends on the chosen slicing orientation:

- **circ-long:** sections aligned with the ventricular circumferential–longitudinal plane. The in-plane f orientation and through-thickness s direction enable near-planar fiber alignment. We consider both aligned and off-axis variants depending on their angular deviation from the square edge. This slab specimen type aligns with the biaxial tension testing slabs studied by [11].
- **circ-rad:** sections cut in the circumferential–radial plane. These samples exhibit a transmural fiber rotation from approximately -60° at the epicardium to $+60^\circ$ at the endocardium, while the sheet direction s remains in-plane and radially aligned.
- **rad-heli:** samples based on a radial-helical cut. Given the natural transmural variation of the myofiber angle f from -60° in the sub-epicardium to $+60^\circ$ in the sub-endocardium [63], this configuration places all three microstructural directions (f, s, n) approximately within the sample plane by rotating the sample an additional 45° along the radial axis. The resultant fiber orientation ranges from -15° up to 105° , aligning the f fiber in the sample plane near the bottom edge of the sample and aligning the n fiber in the sample plane near the top edge.

To investigate the influence of geometric heterogeneity, we introduce a second set of specimens with a central circular occlusion with a radius of 1 mm, see Appendix A. These samples are expected to introduce additional deformation heterogeneity that we hypothesize may improve constitutive parameter identifiability under limited data conditions, e.g., when inferring orthotropic behavior from a single biaxial tensile test.

3.2. Biaxial loading emulation

We simulate a digital volume correlation experiment by modeling a biaxial loading protocol on the microstructurally and geometrically homogeneous and heterogeneous tissue slabs described above using the finite element method (FEM) implemented in ABAQUS/Standard [64], see for example [26]. Our virtual tissue slabs are subjected to displacement-controlled symmetric biaxial loading, with loading ratios $\lambda_1 : \lambda_2 = (1 : 2), (1 : 1), (2 : 1)$ defined in terms of the prescribed edge stretches along the two in-plane loading directions. The maximum stretch applied to the samples is 15% of the initial edge length, consistent with maximal values used in experiments [11]. We use linear tetrahedral elements to discretize the domain and record nodal displacements along with reaction forces for a sequence of n_t load steps (see Figure A.1)

To define the constitutive response, we use the local volume change $J = \det(\mathbf{F})$ and multiplicatively decompose the deformation gradient \mathbf{F} (5) into its volumetric \mathbf{F}^{vol} and isochoric $\bar{\mathbf{F}}$ parts [65],

$$\mathbf{F} = \mathbf{F}^{\text{vol}} \bar{\mathbf{F}} \quad \text{with} \quad \mathbf{F}^{\text{vol}} = J^{\frac{1}{3}} \mathbf{I} \quad \text{and} \quad \bar{\mathbf{F}} = J^{-\frac{1}{3}} \mathbf{F}. \quad (26)$$

We then introduce the following deformation (pseudo-)invariants [66, 67]:

$$\begin{aligned} \bar{I}_1 &= [\bar{\mathbf{F}}^T \bar{\mathbf{F}}] : \mathbf{I} \\ \bar{I}_{4ff} &= [\bar{\mathbf{F}}^T \bar{\mathbf{F}}] : [\mathbf{f}^0 \otimes \mathbf{f}^0] \\ \bar{I}_{4nn} &= [\bar{\mathbf{F}}^T \bar{\mathbf{F}}] : [\mathbf{n}^0 \otimes \mathbf{n}^0] \\ \bar{I}_{4fs} &= [\bar{\mathbf{F}}^T \bar{\mathbf{F}}] : [\mathbf{f}^0 \otimes \mathbf{s}^0] \end{aligned} \quad (27)$$

where $\mathbf{f}^0, \mathbf{s}^0, \mathbf{n}^0$ denote the local microstructure fiber, sheet, and normal unit vector orientations in the undeformed reference configuration. We adopt the orthotropic, compressible Holzapfel-Ogden (HO) material model [14, 15] using the following strain energy density function:

$$\begin{aligned} \psi(\mathbf{F}, \boldsymbol{\theta}) &= \frac{a}{2b} \left[\exp(b(\bar{I}_1 - 3)) - 1 \right] + \sum_{i=f,n} \frac{a_i}{2b_i} \left[\exp\left(b_i (\bar{I}_{4ii} - 1)^2\right) - 1 \right] \\ &+ \frac{a_{fs}}{2b_{fs}} \left[\exp(b_{fs} \bar{I}_{4fs}^2) - 1 \right] + \frac{K}{2} \left(\frac{J^2 - 1}{2} - \ln J \right) \end{aligned} \quad (28)$$

to compute the First Piola Kirchhoff stress tensor \mathbf{P} following (6). This variation of the HO-model was implemented using the recently proposed universal user material subroutine in Abaqus [52].

In (28), $\theta = \{a, b, a_f, b_f, a_n, b_n, a_{fs}, b_{fs}, K\}$ (see Table 1) denotes the to-be-inferred ground-truth material parameters. The Macaulay brackets $\langle x \rangle$ ensure that fiber and sheet term strain energy contributions activate only under tension [68, 69, 52]. Lastly, a bulk modulus is chosen based on the distribution of J in the circ-long-hom samples and common compressibility considerations of the myocardium [70, 71] to limit volumetric strains while retaining numerical stability.

To quantify how microstructural and geometric heterogeneity enrich the deformation space relevant for inference, Figures 4–5 report the resulting distributions of the key invariants activated under biaxial loading, which motivates our single-test identification setup.

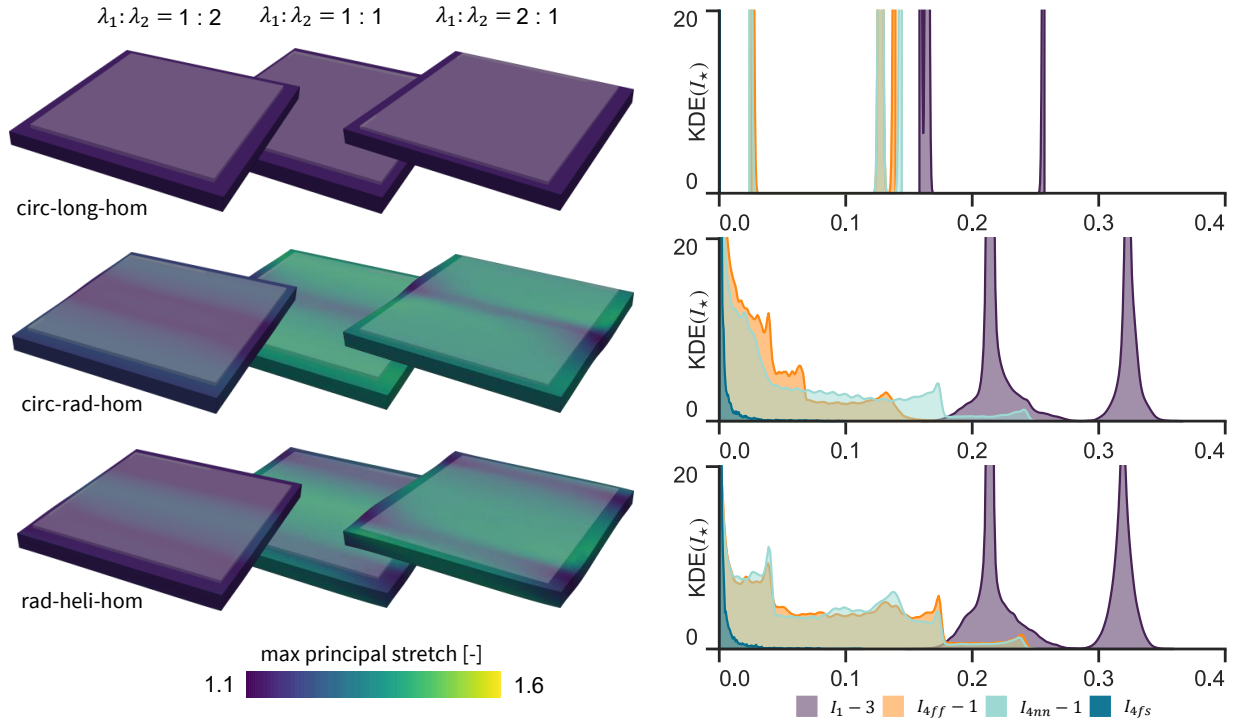


Figure 4: **Deformation profiles of geometrically homogeneous tissue slabs with varying microstructural heterogeneity.** Maximum principal stretches are shown for circ-long-hom (top row), circ-rad-hom (middle row), and rad-heli-hom (bottom row) specimens subjected to biaxial loading protocols ($\lambda_1 : \lambda_2 = (1 : 2), (1 : 1), (2 : 1)$) up to $\lambda^{\max} = 1.15$. Rightmost columns display distributions of invariants $I_1 - 3$, $I_{4ff} - 1$, $I_{4nn} - 1$, and I_{4fs} for each specimen type respectively using approximated kernel density estimations denoted as $\text{KDE}(I_*)$. The kernel density estimation is truncated at an arbitrary level of 20 to show the spread of the invariants more clearly.

Figure 4 presents the deformation response of geometrically homogeneous slabs with varying microstructural architectures. The qualitative results of the maximum principal stretch are shown for all loading conditions and homogeneous tissue samples. On the right side of the figure we show kernel density estimations of the biaxially activated invariants, truncated at 20 to visualize the spread of these invariants. The *circ-long-hom* configuration represents a classic homogenized myocardial sample, as excised by [11], with assumed uniform fiber-sheet-normal orientations. Under biaxial loading, this results in a uniform deformation pattern with isotropic invariants I_1 ranging from 3.158 to 3.257 across the three loading protocols. Anisotropic contributions are moderate, with I_{4ff} and I_{4nn} spanning ranges from 1.025 to 1.139 and 1.024 to 1.144 respectively. Fiber-sheet shear contributions remain negligible, with I_{4fs} limited to 0.000 up to machine precision. Introducing transmural fiber variation in the *circ-rad-hom* slab increases local deformation heterogeneity. The isotropic deformation invariant I_1 expands to a broader range of 3.160 to 3.367, while I_{4ff} and I_{4nn} reach 1.194 and 1.252, respectively. Notably, fiber-sheet shear contributions increase, with I_{4fs} reaching up

to 0.099. In the *rad-heli-hom* specimen, which introduces a more asymmetric helical fiber distribution, deformation heterogeneity is further amplified. The isotropic invariant I_1 ranges from 3.147 to 3.359, while I_{4ff} increases significantly, spanning up to 1.248. The I_{4nn} component reaches 1.251, and fiber-sheet shear contributions grow to 0.114. The distributions of invariants shown in the right column of Figure 4 emphasize these trends. The circ-long-hom specimen exhibits single homogeneous singular values for I_{4ff} and I_{4nn} , while I_{4fs} remains zero. In contrast, circ-rad-hom and rad-heli-hom configurations display broader distributions across all invariants, particularly for fiber-sheet shear deformations. Consistent with these observations, we note tissue bulging effects in the thickness direction. Circ-rad configurations exhibit bulging centrally, whereas rad-heli configurations deform near the specimen edges. In particular, the rad-heli-hom configuration shows noticeable thickness bulging coinciding with bands of reduced strain, where fibers align in-plane. Overall, microstructure-induced heterogeneity alone enriches the activated invariant space under a single biaxial protocol, which motivates using these slabs as training configurations in this study.

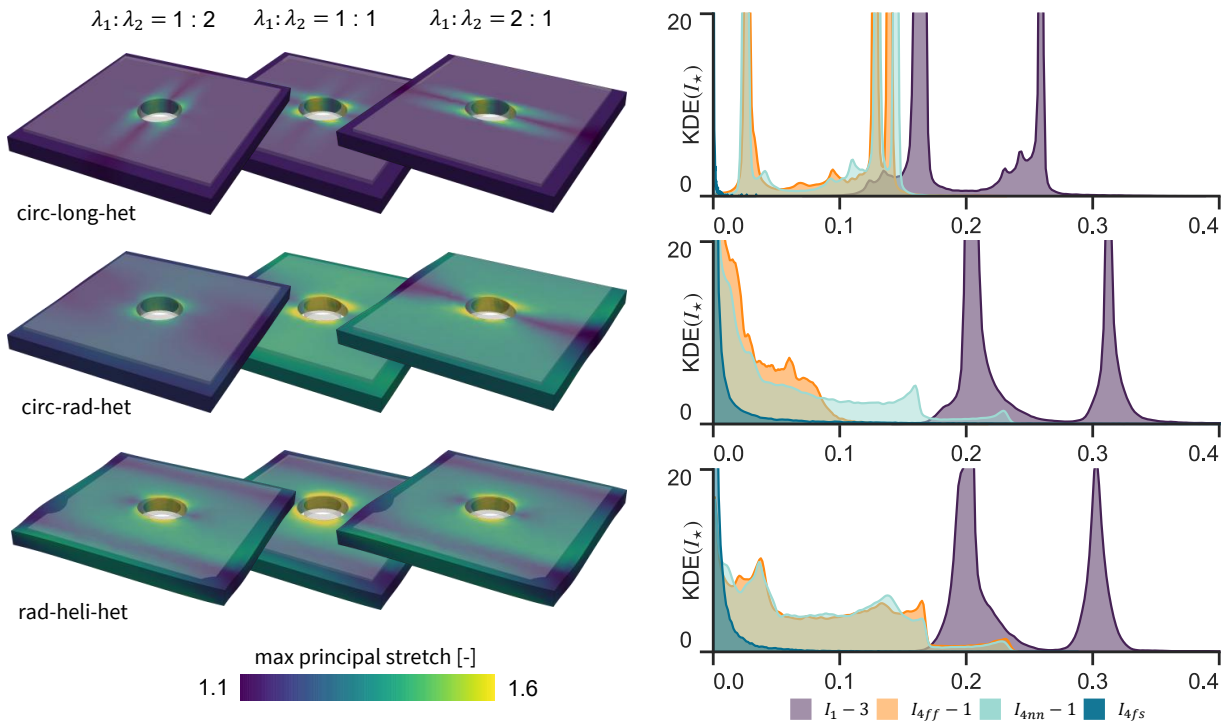


Figure 5: **Deformation profiles of geometrically heterogeneous tissue slabs with varying microstructural heterogeneity.** Maximum principal stretches circ-long-het (top row), circ-rad-het (middle row), and rad-heli-het (bottom row) specimens under biaxial loading ($\lambda_1 : \lambda_2 = (1 : 2), (1 : 1), (2 : 1)$). Invariant distributions of $I_1 - 3$, $I_{4ff} - 1$, $I_{4nn} - 1$, and I_{4fs} are shown in the rightmost panels using approximated kernel density estimations denoted as $\text{KDE}(I_*)$. The kernel density estimation is truncated at an arbitrary level of 20 to show the spread of the invariants more clearly.

Figure 5 illustrates the deformation response of geometrically heterogeneous slabs, where a central occlusion is combined with varying microstructural organization. In the *circ-long-het* specimen, geometric heterogeneity alone induces significant deformation diversity. The isotropic invariant I_1 spans from 3.070 to 3.390, with I_{4ff} and I_{4nn} reaching up to 1.232 and 1.209, respectively. Fiber-sheet shear contributions, represented by I_{4fs} , remain limited, peaking at 0.034. Adding microstructural heterogeneity in the *circ-rad-het* configuration further amplifies deformation heterogeneity. Here, I_1 varies between 3.141 and 3.5477, while I_{4ff} and I_{4nn} attain maximum principal stretches of 1.218 and 1.243 respectively. Notably, fiber-sheet shear contributions increase substantially, with I_{4fs} rising to 0.4342. In the *rad-heli-het* specimen, characterized by asymmetric helical fiber variation and geometric heterogeneity, isotropic I_1 deformation spans 3.136 to 3.518. Anisotropic contributions reach 1.242 for I_{4ff} , 1.241 for I_{4nn} , and 0.289 for the fiber-sheet shear term I_{4fs} , which confirms this configuration as the most mechanically diverse. The distributions of invariants reflect these differences. The circ-long-het slab shows moderate spreading compared to its homogeneous

counterpart, but fiber-sheet shearing remains limited. In contrast, the circ-rad-het and rad-heli-het configurations exhibit pronounced broadening in all invariants, particularly in I_{4fs} , underscoring the synergistic effect of combined geometrical and microstructural heterogeneities. Similar to the homogeneous cases, bulging effects are evident. Circ-rad configurations exhibit central bulging, while rad-heli configurations deform near specimen edges. The rad-heli-het specimen shows the most pronounced bulging, exceeding initial thickness. Localized deformation bands with reduced strain are again visible, while regions surrounding the central occlusion display elevated strains, highlighting the amplification of local deformation due to geometric discontinuities. These observations reinforce the rationale for using such heterogeneous configurations as training specimens, enhancing parameter identifiability through enriched mechanical diversity.

4. Inference results and robustness to measurement noise

4.1. Noise-free inference: identifiability gains from microstructural and geometrical heterogeneity

Figures 6 and 7 summarize the inference performance of our framework in recovering the ground-truth HO parameter set θ_{gt} (Table 1) based on combined full-field deformation and reaction force data. Each figure shows, from top to bottom: (i) the evolution of the inferred parameters' guide location μ_θ over optimization epochs, (ii) the corresponding absolute relative errors e_{μ_θ} , (iii) final relative errors after convergence, and (iv) posterior distributions $\tilde{\theta}$, scaled to highlight skewness and relative spread. Here, we highlight posterior distributions in color when the unbiased skewness value $|s_{\tilde{\theta}}|$ is strictly greater than 0.5. We define the following four metrics: the relative point error metric \hat{e}_θ between the mean of the underlying and untruncated normal distribution and the ground truth, and the relative error e_θ between samples from the posterior and the ground truth:

$$\hat{e}_\theta = \frac{\mu_\theta - \theta_{\text{gt}}}{\theta_{\text{gt}}} \quad e_\theta = \frac{\theta - \theta_{\text{gt}}}{\theta_{\text{gt}}} \quad (29)$$

Here, we define $\mu_\theta = \mu^q$ as the mean of the underlying untruncated normal distribution used in the guide distribution. Furthermore, we define the unbiased skewness $s_{\tilde{\theta}}$:

$$s_{\tilde{\theta}} = \frac{\sqrt{N(N-1)}}{N-2} \cdot \frac{\frac{1}{N} \sum_{n=1}^N (\tilde{\theta}_n - \mu_{\tilde{\theta}})^3}{\left(\frac{1}{N} \sum_{n=1}^N (\tilde{\theta}_n - \mu_{\tilde{\theta}})^2\right)^{3/2}} \quad \text{with} \quad \tilde{\theta} = \frac{\theta - \mu_\theta}{\mu_\theta} \quad (30)$$

with $\tilde{\theta}$ denoting the relative error between samples taken from the guide distribution and the scaled posterior, $\mu_{\tilde{\theta}}$ denoting the mean of the distribution $\tilde{\theta}$, and N equaling the number of samples drawn from the posterior distribution. Unless stated otherwise, we draw $N = 1,000$ samples from the inferred guide distribution shown in the bottom rows of Figures 6 and 7, respectively, to visualize the shape, mean, and spread of the approximated posterior distribution. For completeness, the full set of converged parameter estimates, posterior scales (the standard deviation of the underlying and untruncated normal distribution), and relative errors for all six training specimens is reported in Appendix B (Tables B.3–B.4). In the main text, we therefore focus on the parameter groups that drive the qualitative differences between Figures 6 and 7, and summarize the remaining terms compactly.

Focusing on the *geometrically homogeneous* specimens (Figure 6), the plots show rapid convergence and narrow posteriors for the isotropic (a, b, K) and primary anisotropic (a_f, b_f, a_n, b_n) parameter groups across all three microstructural settings. Quantitatively, these parameters reach small final deviations, with the largest magnitudes remaining below 2.3×10^{-4} in this homogeneous-geometry group (Table B.4). In contrast, the fiber-sheet shear-coupling terms (a_{fs}, b_{fs}) are the dominant outliers. In the fully homogeneous *circ-long-hom* specimen, the shear-coupling terms remain poorly identified, with large final errors ($\hat{e}_{a_{fs}} = -1.42 \times 10^2$ and $\hat{e}_{b_{fs}} = 9.20 \times 10^{-1}$; Table B.4). Introducing transmural and helical fiber variation improves identifiability of a_{fs} substantially (from $\mathcal{O}(10^2)$ to $\mathcal{O}(10^{-3}-10^{-2})$; Table B.4), while b_{fs} remains the least accurate inferred parameter in the homogeneous-geometry group (e.g., $\hat{e}_{b_{fs}} = 1.72 \times 10^{-1}$ for *circ-rad-hom* and 3.74×10^{-1} for *rad-heli-hom*). Notably, b_{fs} also converges more slowly than the remaining parameters: it stabilizes only after $\sim 3 \times 10^4$ epochs in *circ-rad-hom*, and it shows no clear plateau by 10^5 epochs

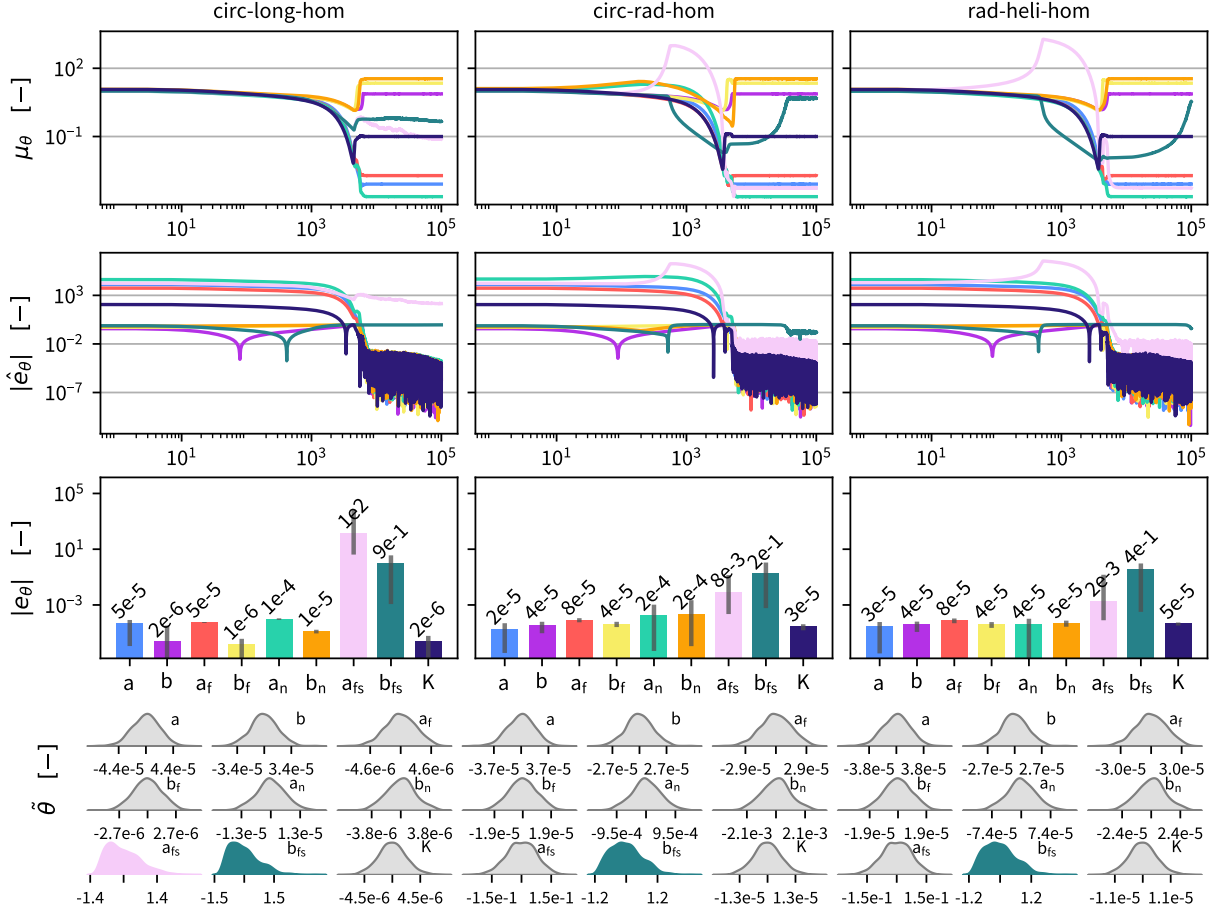


Figure 6: **Noise-free parameter inference on geometrically homogeneous tissue slabs with varying microstructure.** From left to right: circ-long-hom, circ-rad-hom, and rad-heli-hom specimens. From top to bottom: (i) evolution of inferred material parameters θ over optimization epochs, (ii) evolution of absolute relative location parameter errors $|\hat{e}_\theta|$, (iii) absolute relative errors $|e_\theta|$ at the final epoch with corresponding 95% credibility interval, and (iv) rescaled posterior distributions $\hat{\theta}$ (drawn from the variational guide). The plots show rapid convergence and small final errors for most parameters across all three specimens, while the shear-coupling parameters (a_{fs} , b_{fs}) display slower convergence and broader posteriors in several cases. Distributions are shown in grayscale when the absolute unbiased skewness satisfies $|s_{\hat{\theta}}| < 0.5$.

in *rad-heli-hom*, whereas most other parameters stabilize within $\sim 8 \times 10^3$ epochs (rows (i)–(ii)). These trends are consistent with the broader and more skewed posteriors for (a_{fs} , b_{fs}) in Figure 6 (bottom row).

For the *geometrically heterogeneous* specimens (Figure 7), the plots show stable convergence across parameter groups and generally narrower posterior spreads than in Figure 6. For the isotropic and primary anisotropic parameters, final deviations remain small overall, with the largest magnitudes staying below 5×10^{-4} across the heterogeneous-geometry group (Table B.4). The most pronounced quantitative change occurs in the inferred shear-coupling parameters. With combined geometric heterogeneity and fiber rotation, both a_{fs} and b_{fs} converge to small final deviations: in *circ-rad-het*, $\hat{e}_{a_{fs}} = -2.52 \times 10^{-3}$ and $\hat{e}_{b_{fs}} = -1.54 \times 10^{-3}$, and in *rad-heli-het*, $\hat{e}_{a_{fs}} = -1.14 \times 10^{-3}$ and $\hat{e}_{b_{fs}} = 6.90 \times 10^{-3}$ (Table B.4). In contrast, without fiber rotation (*circ-long-het*), b_{fs} remains comparatively inaccurate ($\hat{e}_{b_{fs}} = 0.879$), consistent with the broader posterior in the corresponding column of Figure 7. Compared with the homogeneous-geometry cases in Figure 6, the rotated-fiber heterogeneous specimens (*circ-rad-het* and *rad-heli-het*) reach a stable b_{fs} trajectory with small final deviations within $\mathcal{O}(10^4)$ epochs ($\sim 5 \times 10^3$ and $\sim 10^4$ epochs, respectively), rather than requiring $\sim 3 \times 10^4$ to $> 10^5$ epochs, consistent with the tighter posterior spreads in row (iv).

Across both Figures 6 and 7, several parameters exhibit non-monotonic transients before converging. In particular,

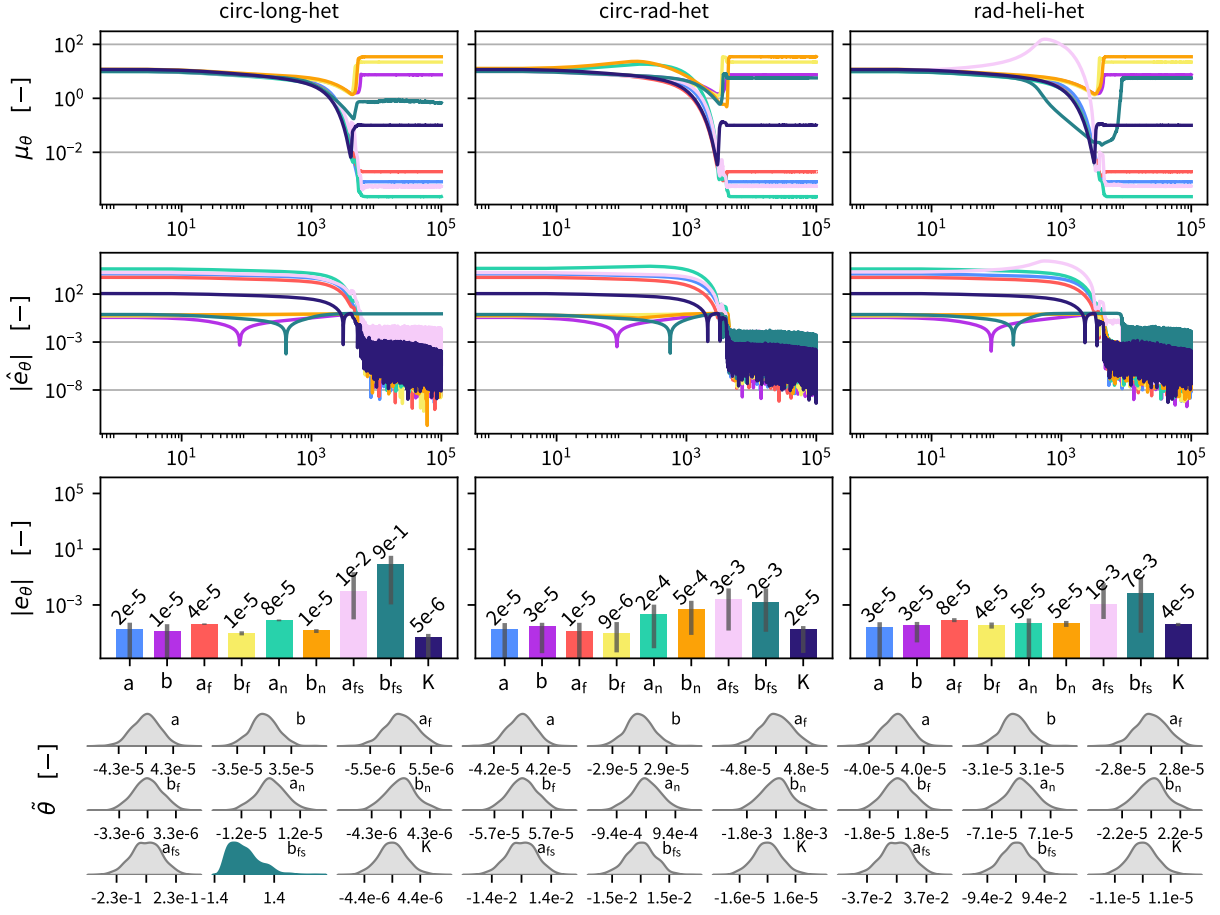


Figure 7: **Noise-free parameter inference on geometrically heterogeneous tissue slabs with varying microstructure.** From left to right: circ-long-het, circ-rad-het, and rad-heli-het specimens. From top to bottom: (i) evolution of inferred material parameters θ over optimization epochs, (ii) evolution of absolute relative location parameter errors $|\hat{e}_\theta|$, (iii) absolute relative errors $|e_\theta|$ at the final epoch with corresponding 95% credibility interval, and (iv) rescaled posterior distributions $\hat{\theta}$ (drawn from the variational guide). The plots show stable convergence for all parameter groups across the three specimens, and the posterior samples indicate narrower spreads for the shear-coupling parameters (a_{fs} , b_{fs}) compared with the homogeneous counterparts. Distributions are shown in grayscale when the absolute unbiased skewness satisfies $|s_{\hat{\theta}}| < 0.5$.

multiple traces (including b , b_f , a_n , and a_{fs}) show a decrease after roughly 10^3 epochs, followed by recovery towards their converged values by $O(10^4)$ epochs. Consistent excursions appear in the error plots over the same epoch range, reflecting epochs where the inferred trajectories pass through the ground-truth value (i.e., where the signed relative deviation changes sign) without immediately stabilizing. This behavior is consistent with strong parameter coupling and a nonconvex loss landscape in nonlinear orthotropic inference, where the optimizer can traverse multiple basins before stabilizing.

4.2. Robustness to displacement noise

We next assess robustness to displacement measurement noise by perturbing the measured full-field kinematics with additive Gaussian white noise at two levels: low ($\sigma_u = 1 \times 10^{-4}$ mm) and high ($\sigma_u = 1 \times 10^{-3}$ mm). We intentionally avoid modeling spatially correlated noise here. Instead, we use spatially uncorrelated Gaussian white noise as a conservative stress test of the inference framework, with noise magnitudes chosen in line with prior inverse and Bayesian identification studies [30, 31, 32, 72]. Realistic displacement fields, for example those obtained with DIC, typically exhibit spatial correlations. Related work has incorporated correlated noise models or DIC-aware fictitious noise to mimic these effects more closely [29, 73]. In this study, we deliberately adopt the simpler white-noise approximation to probe robustness under coarse, worst-case perturbations, and we apply it to the *geometrically heterogeneous* training specimens, since these provided the most reliable baseline inference performance in the noise-free setting (Section 4.1).

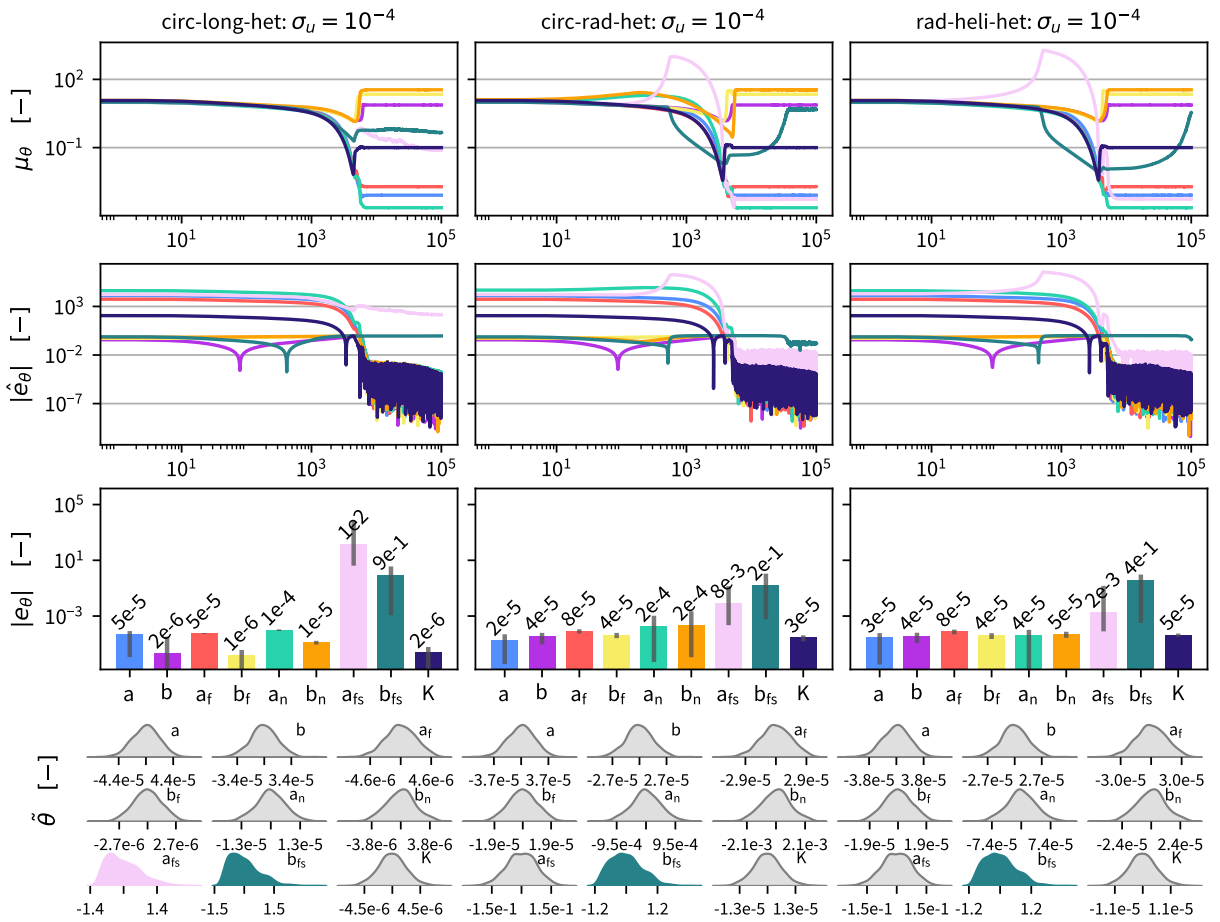


Figure 8: **Parameter inference on geometrically and microstructurally heterogeneous tissue slabs under low displacement measurement noise.** From left to right: circ-long-het, circ-rad-het, and rad-heli-het specimens. From top to bottom: (i) evolution of inferred material parameters θ over optimization epochs, (ii) evolution of absolute relative location parameter errors $|\hat{e}_\theta|$, (iii) absolute relative errors $|e_\theta|$ at the final epoch with corresponding 95% credibility interval, and (iv) rescaled posterior distributions $\hat{\theta}$ (drawn from the variational guide). The plots show that most parameters maintain stable convergence under low noise, while a_{fs} and b_{fs} exhibit the largest variability across specimens, reflected by slower convergence and broader posteriors. Here, uncorrelated Gaussian displacement noise with standard deviation $\sigma_u = 10^{-4}$ mm is added to the full-field kinematics. Distributions are shown in grayscale when the absolute unbiased skewness satisfies $|s_{\hat{\theta}}| < 0.5$.

Figure 8 summarizes inference under low displacement noise for the three geometrically heterogeneous training specimens. Across all three microstructural settings, the trajectories in rows (i) and (ii) indicate that the low-noise setting largely preserves the convergence patterns of the noise-free heterogeneous baseline in Figure 7, and differences emerge

most clearly in the shear-coupling terms. For *circ-long-het*, final relative errors for isotropic and primary anisotropic parameters stay within a narrow band, with representative values between 10^{-4} and 5×10^{-3} (Table C.7). In contrast, the parameter trajectory for a_{fs} does not settle to a clear plateau in row (i), and b_{fs} exhibits increased stochasticity together with a mild downward drift. The corresponding relative errors for the shear-coupling terms are of order one, with $|\hat{e}_{a_{fs}}| \approx 1$ and $|\hat{e}_{b_{fs}}| \approx 0.9$. This behavior is mirrored in the posterior samples in row (iv), which show pronounced skewness and visible truncation for (a_{fs}, b_{fs}) , consistent with elevated uncertainty and weak practical identifiability under this noise level. Whereas in the noise-free heterogeneous setting (Figure 7) the shear parameter a_{fs} could still be identified up to a relative error on the order of 10^{-2} , the low-noise case now produces errors for both a_{fs} and b_{fs} of the same order of magnitude as their true values. In the helically distributed fiber specimens *circ-rad-het* and *rad-heli-het*, the posterior samples in row (iv) do not exhibit comparable skewness or truncation for the inferred parameters. Compared with the noise-free case, the final relative errors for isotropic and primary anisotropic parameters are slightly higher, remaining mostly between 5×10^{-3} and 10^{-1} for *circ-rad-het* and between 3×10^{-4} and 2×10^{-2} for *rad-heli-het* (excluding a_{fs} and b_{fs}), while the majority of parameters still converge to clearly defined plateaus in rows (i) and (ii). For the shear-coupling terms, the posterior shapes of (a_{fs}, b_{fs}) become more regular in row (iv), yet their error traces in row (ii) plateau at comparatively elevated levels. In the noise-free case (Figure 7), we achieved rotated-fiber shear-coupling errors $|\hat{e}_{a_{fs}}|$ of order 10^{-3} and $|\hat{e}_{b_{fs}}|$ of at most 10^{-2} in the *circ-rad-het* and *rad-heli-het* specimens (Table B.4). Under low noise here, these errors increase to magnitudes between roughly 5×10^{-1} and order one, with the largest outlier observed for b_{fs} in *rad-heli-het* (Table C.7). Strikingly, the shear-coupling parameters stabilize in the *circ-rad-het* and *rad-heli-het* configurations after roughly 5,000 and 40,000 epochs respectively, even though their relative errors remain high. Combined with the lack of skewness and truncation in their posteriors, this pattern is consistent with the parameters having moved away from the prior and having settled in a suboptimal local minimum under low-noise conditions.

Figure 9 assesses parameter inference under high displacement measurement noise ($\sigma_u = 10^{-3}$ mm) for the three geometrically heterogeneous specimens, using the same layout as in Figure 8. Relative to the low-noise case, the trajectories in rows (i) and (ii) show a marked loss of stability and accuracy, most prominently in the shear-coupling parameters (a_{fs}, b_{fs}) . Across all three specimens, these shear terms no longer attain reliable plateaus, their estimates for a_{fs} collapse towards numerical near-zero values, and the corresponding relative errors remain of order one (Table C.7). In addition, the primary anisotropic sheet-direction parameters (a_n, b_n) in the *circ-rad-het* specimen fail to settle to stable values and reach relative errors close to unity, indicating a breakdown of identifiability in this parameter group under high noise. By contrast, the isotropic and primary anisotropic parameters remain comparatively more robust in *circ-long-het*, where final relative errors for these parameters mostly lie between 10^{-3} and 5×10^{-2} . In the *rad-heli-het* specimen, these relative parameter errors fall between 5×10^{-2} and 10^{-1} (Table C.7). The *circ-rad-het* configuration clearly performs worst overall, with many isotropic and primary anisotropic parameters exhibiting relative errors in the range 2×10^{-1} to 1, representing a sharp degradation compared with both the noise-free and low-noise cases. Similar to the low-noise setting, parameters that do stabilize under high noise typically do so around 8,000 epochs for *circ-long-het* and *circ-rad-het*, whereas the *rad-heli-het* specimen requires up to about 10,000 epochs for its stable parameter groups. Appendix C provides the corresponding noisy hyperparameter and constitutive parameter estimates, together with their relative errors and posterior scale parameters (Tables C.5–C.7), which quantitatively underpin the trends observed in Figures 7–9.

Comparing Figures 7, 8, and 9 show a clear, parameter-selective degradation of identifiability as displacement noise increases from zero to low to high levels. In the noise-free heterogeneous baseline (Figure 7), isotropic and primary anisotropic parameters achieve small final deviations, with $|\hat{e}_\theta|$ typically below 5×10^{-4} , while the shear-coupling terms (a_{fs}, b_{fs}) are already more sensitive in *circ-long-het* but remain well identified in *circ-rad-het* and *rad-heli-het* (Table B.4). Under low noise (Figure 8), these isotropic and primary anisotropic errors increase by roughly one to two orders of magnitude yet mostly remain below 10^{-1} , whereas the shear-coupling errors in *circ-long-het*, *circ-rad-het*, and *rad-heli-het* rise to order one or larger, consistent with the broadened and, in some cases, truncated posteriors for (a_{fs}, b_{fs}) . At high noise (Figure 9), this trend intensifies: the shear-coupling parameters lose practical identifiability in all three specimens, with $|\hat{e}_{a_{fs}}|$ and $|\hat{e}_{b_{fs}}|$ remaining of order one and the corresponding posterior samples strongly skewed, while selected primary anisotropic parameters in *circ-rad-het* (notably a_f , a_n , and b_n) also exhibit near-unity relative errors and non-stabilizing trajectories. By contrast, most isotropic parameters and the bulk modulus K retain comparatively moderate deviations even at the highest noise level, particularly in *circ-long-het* and *rad-heli-het*,

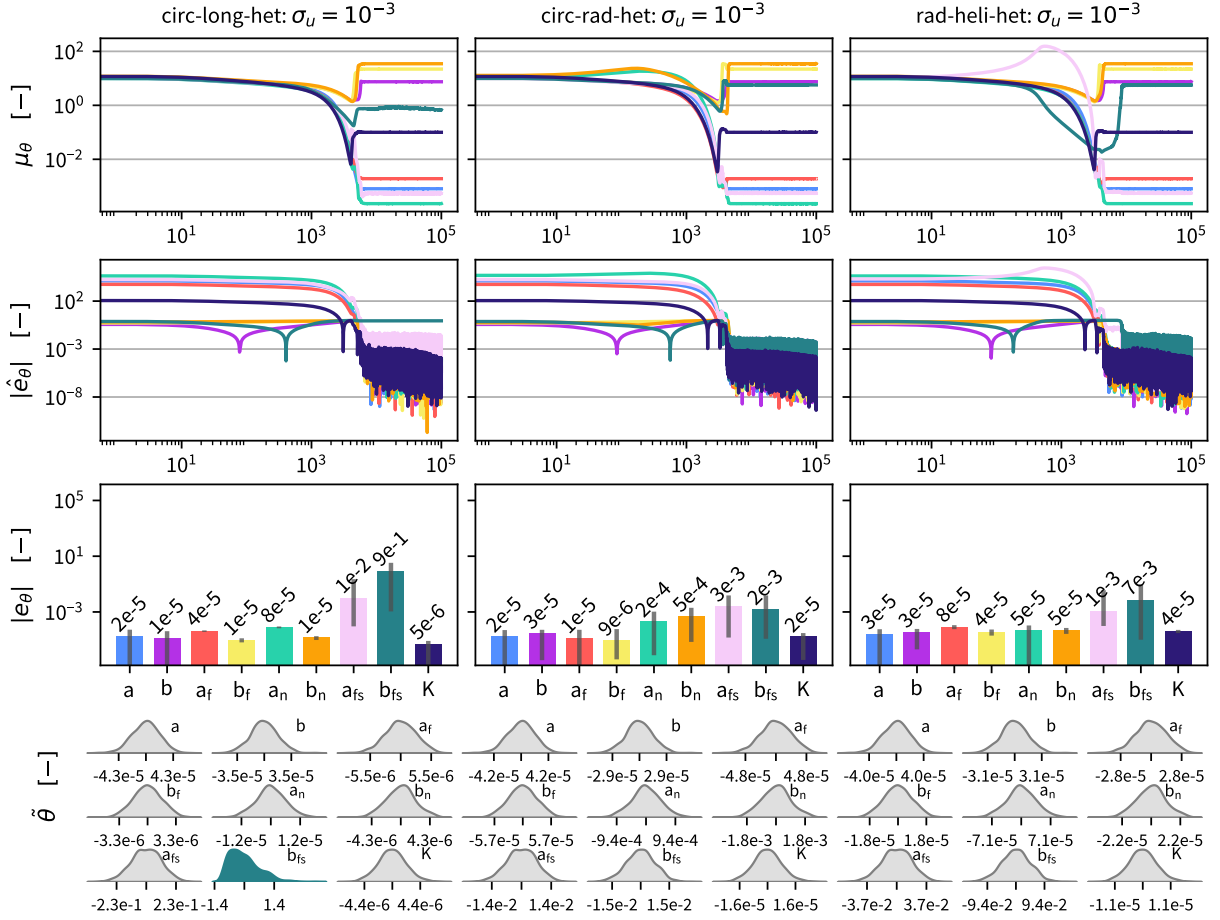


Figure 9: **Parameter inference on geometrically and microstructurally heterogeneous tissue slabs under high displacement measurement noise.** From left to right: circ-long-het, circ-rad-het, and rad-heli-het specimens. From top to bottom: (i) evolution of inferred material parameters θ over optimization epochs, (ii) evolution of absolute relative location parameter errors $|\hat{e}_\theta|$, (iii) absolute relative errors $|e_\theta|$ at the final epoch with corresponding 95% credibility interval, and (iv) rescaled posterior distributions $\hat{\theta}$ (drawn from the variational guide). The plots show increased variability and slower stabilization for several parameters compared with the low-noise case, with the shear-coupling parameters (a_{fs} , b_{fs}) exhibiting the largest spread in the posterior samples across specimens. Here, displacement noise with standard deviation $\sigma = 10^{-3}$ mm is added to the full-field kinematics. Distributions are shown in grayscale when the absolute unbiased skewness satisfies $|s_\theta| < 0.5$.

indicating a degree of robustness in the volumetric and baseline stiffness sector despite the pronounced degradation in shear-related and directional anisotropic terms.

5. Validation beyond training

We now assess how well parameter sets inferred from single-shot heterogeneous biaxial tests generalize beyond the specific training protocol. To this end, we first compare Cauchy stress responses of inferred parameter sets under classical homogeneous uni-modal deformation modes against the ground-truth parameterized Holzapfel–Ogden law. Subsequently, we probe more complex mixed-modal deformation states, sampled from a physiologically constrained invariant space, and compare the resulting strain energy between inferred and ground-truth parameters to assess generalization under heterogeneous load paths.

5.1. Uni-modal deformation mode validation

We reproduce homogeneous, uni-modal loading protocols, i.e. classical incompressible biaxial tension and triaxial shear tests, following the experimental protocols of [10, 11]. We consider incompressible biaxial tension, where λ_f and λ_n are prescribed and λ_s follows from incompressibility, and triaxial shear tests, where the principal stretches are fixed to unity and a single shear component is activated per test. The resulting stress expressions are summarized in Appendix D. Constitutive parameters inferred from our unsupervised single-shot heterogeneous biaxial protocol are then used to assess, in a controlled fashion, the predictive capability of the proposed framework relative to established multi-modal calibration pipelines for myocardial tissue [12, 15, 16, 26].

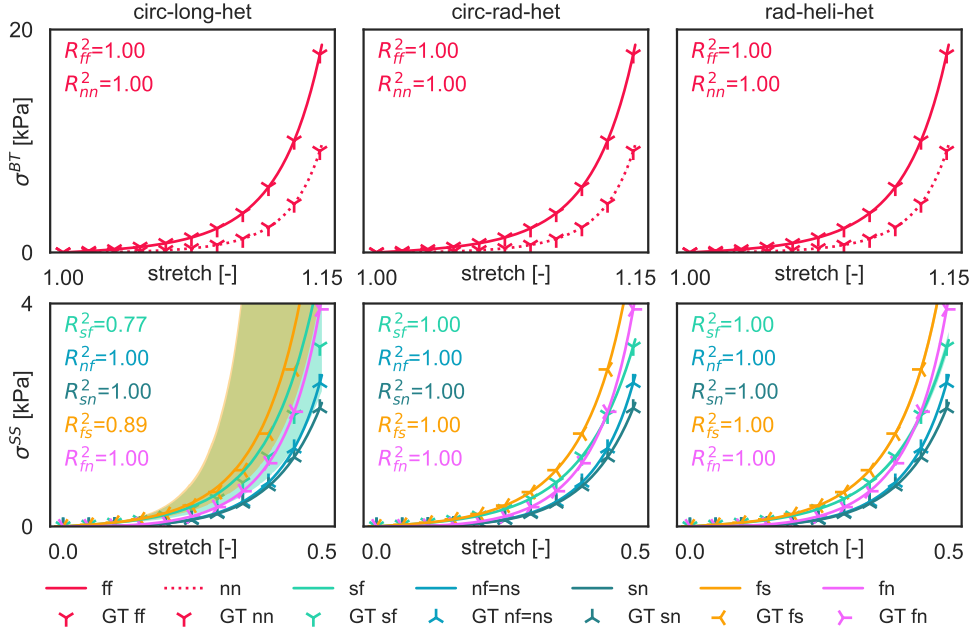


Figure 10: **Noise-free single-shot inference validation under homogeneous uni-modal loading.** Cauchy stresses predicted by the ground-truth HO parameter set (tri markers) and by the inferred noise-free single-shot full-field posterior (shaded 95% credible intervals) for three heterogeneous configurations: circ-long-het (left), circ-rad-het (middle), and rad-heli-het (right). Rows correspond to classical incompressible biaxial tension and triaxial shear modes. Panel-wise R^2 values quantify agreement between posterior mean predictions and ground-truth stresses. Noise-free inference generalizes perfectly across all modes for circ-rad-het and rad-heli-het ($R^2 \approx 1$ throughout), while circ-long-het shows the largest deviations in cross-fiber shear (σ_{fs} , σ_{sf}).

Figure 10 reports noise-free validation across the three geometrically heterogeneous configurations: circ-long-het (left), circ-rad-het (middle), and rad-heli-het (right). Each column compares Cauchy stresses from the ground-truth parameter set (tri markers) with predictions based on the noise-free single-shot full-field inference parameter sets (shaded 95% credible intervals) under classical biaxial tension and triaxial shear tests. Leveraging parameters inferred from the noise-free *circ-long-het* slab, the inferred biaxial stress-stretch curves match the ground-truth mechanical response of the tissue with $R^2 = 1.00$ for both biaxial tension cases. The inferred nf -, sn -, and ns -shear responses are also indistinguishable from the ground-truth response, whereas the inferred cross-fiber shear behavior shows lower agreement with respect to the ground-truth model, with $R^2 = 0.89$ and $R^2 = 0.77$ for σ_{fs} and σ_{sf} respectively. Aggregated over all tests in this configuration, the overall coefficient of determination amounts to $R^2 = 0.96$. These deviations are consistent with the limited deformational excitation of the I_{4fs} shear-coupling invariant in the circ-long-het specimen (Figure 5) and with the weaker identifiability of (a_{fs}, b_{fs}) observed in the previous section. Leveraging the *circ-rad-het* slab, the inferred constitutive parameter sets perfectly reproduce the ground-truth stresses across all biaxial tension and shear tests with $R^2 = 1.00$ in every panel. Posterior confidence intervals remain tight, indicating precise recovery of the underlying constitutive parameters for this orientation, including the shear-coupling response. Focusing on the *rad-heli-het* specimen, the inferred stress curves again overlay the ground-truth for all biaxial tensile

and shear tests with $R^2 = 1.00$. Overall, the noise-free validation shows that single-shot full-field inference generalizes reliably across all three heterogeneous configurations, with slight deviations confined to cross-fiber shear in the circ-long-het case, which is in agreement with the parameter-level identifiability analysis in Figure 7.

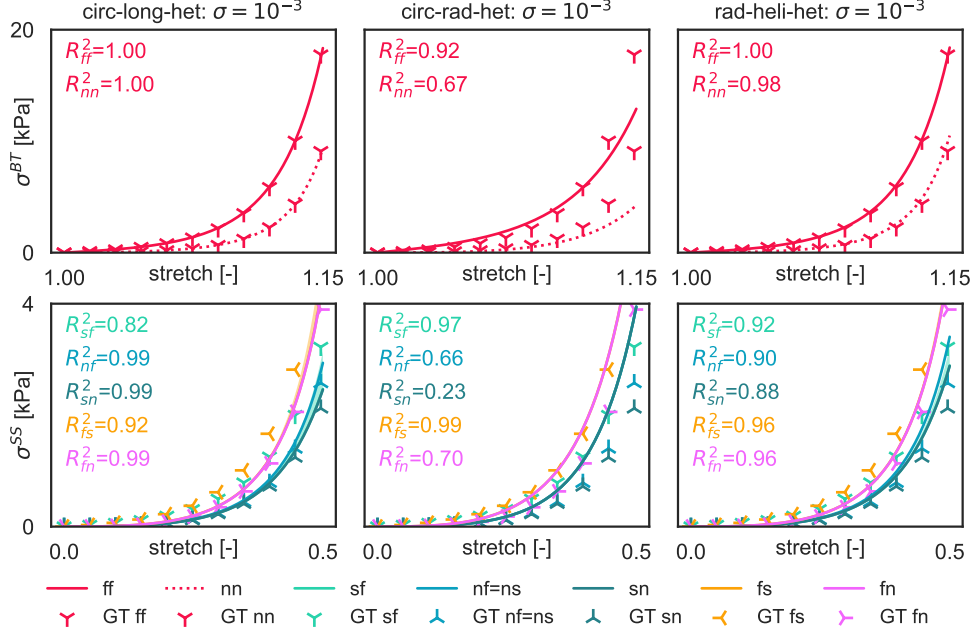


Figure 11: **High-noise single-shot inference validation under homogeneous uni-modal loading.** Cauchy stresses predicted by the ground-truth HO parameter set (tri markers) and by the inferred single-shot full-field posterior under displacement noise $\sigma_u = 10^{-3}$ mm (shaded 95% credible intervals) for circ-long-het (left), circ-rad-het (middle), and rad-heli-het (right). Rows correspond to the same biaxial tension and triaxial shear protocols as in Figure 10. Panel-wise R^2 values quantify agreement between posterior mean predictions and ground-truth stresses. High noise primarily degrades cross-fiber shear predictivity and widens credible intervals, most notably for circ-rad-het, while biaxial tension and non-cross-fiber shear modes remain well captured, particularly for circ-long-het and rad-heli-het.

Figure 11 reports high-noise ($\sigma_u = 10^{-3}$) validation for the same three heterogeneous single-shot slab specimens. Inferring from displacement and reaction force data in the *circ-long-het* specimen, the inferred biaxial tension behavior remains well aligned with the ground-truth, with panel-wise R^2 values close to one. Similarly, the *nf*-, *sn*-, and *ns*-shear responses retain correct magnitude and slope. Noise primarily affects the inferred cross-fiber shear stresses σ_{fs} and σ_{sf} , where credible intervals widen and small systematic deviations between ground-truth and inferred curves appear. Aggregated over all tests in this configuration, the overall coefficient of determination remains high at $R^2 = 0.96$. Leveraging the *circ-rad-het* slab, stresses computed from the high-noise inferred parameter sets no longer match the uni-modal ground-truth responses perfectly. Mean trends are preserved across biaxial and shear protocols, but panel-wise R^2 values are lower than in the *circ-long-het* and *rad-heli-het* configurations, particularly in cross-fiber and sheet-direction shear. Nevertheless, the aggregated coefficient of determination still reaches $R^2 = 0.77$. Lastly, we note the best uni-modal predictive nature of the inferred parameter set from the high-noise *rad-heli-het* specimen, with all panel-wise R^2 -values greater than 0.88 and an aggregated coefficient of determination of $R^2 = 0.93$. Overall, despite elevated displacement noise and the associated degradation in certain parameter estimates reported in Section 4.2, the single-shot stochastic variational inference framework maintains very good quantitative agreement with uni-modal ground-truth stresses across all three heterogeneous configurations, especially in the biaxial tension and non-cross-fiber triaxial shear modes.

5.2. Mixed-modal deformation validation

To probe generalization under mixed deformation modes, we sample deformation states in invariant spaces between the homogeneous loading paths. We draw $(I_1, I_{4ff}, I_{4nn}, I_{4fs})$ uniformly within the minimum and maximum values

induced by the homogeneous protocols in the uni-modal deformation, see also (D.1), and retain only physiologically admissible states. Specifically, we accept samples that satisfy near-incompressibility $0.9999 \leq J \leq 1.0001$ and whose maximum principal Cauchy stress does not exceed 20.3 kPa, consistent with reported peak stresses for left-ventricular biaxial tests on human myocardial tissue [11]. The invariant-to-kinematics reconstruction and stress evaluation used for filtering are detailed in Appendix E. We repeat this procedure until 5,000 admissible mixed-modal states are obtained. Figure 12 illustrates the resulting invariant coverage. The thin sweeping colored arcs represent the uni-

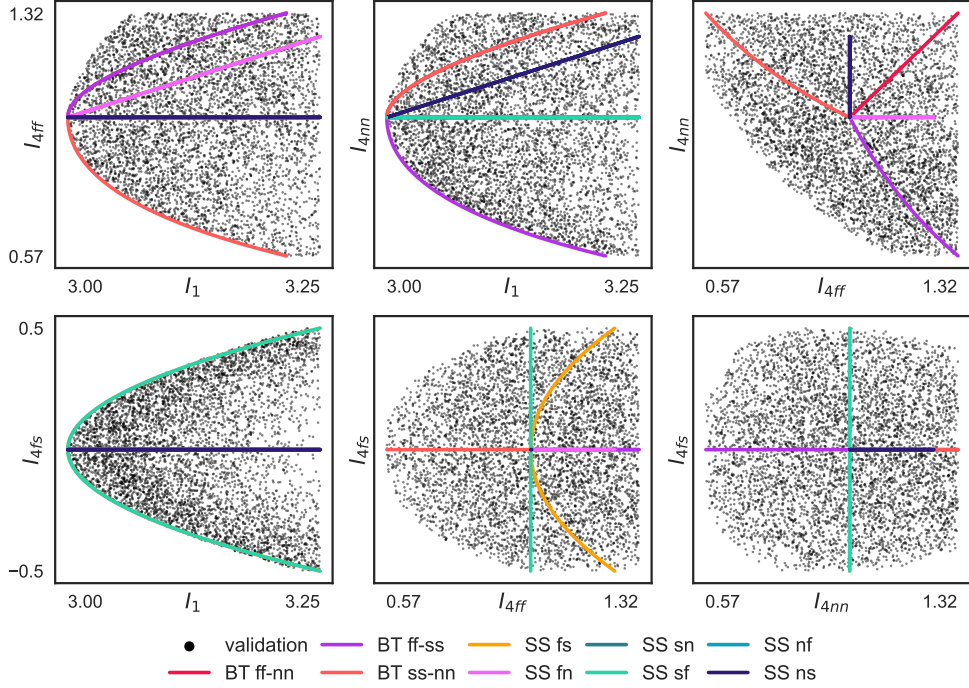


Figure 12: **Mixed-modal validation set construction in invariant space.** Invariant trajectories induced by uni-modal biaxial and single-shear protocols (colored curves) compared with randomly sampled invariant combinations that satisfy (quasi-)incompressibility and a physiological bound on maximum principal stress detailed in Appendix E. The uni-modal protocols excite low-dimensional paths, whereas the accepted multi-modal deformation modes populate the space between these uni-modal paths, yielding mixed-modal deformation states for further and richer out-of-training validation.

modal loading conditions from the previous section, highlighting that these tests excite the invariants along low-dimensional paths. In contrast, our randomly sampled deformation gradients populate the space between these arcs and thus correspond to more complex mixed-modal testing protocols. The accepted samples lie between 3 and 3.25 in I_1 , between 0.57 and 1.32 for I_{4ff} and I_{4nn} , and between -0.5 and 0.5 for I_{4fs} , and they are spread out approximately uniformly within this constrained region. This construction supports the view that the resulting invariant set spans a physiologically relevant range of deformation states that is well suited for out-of-training validation of the inferred versus ground-truth constitutive parameter set.

More specifically, we compute strain energies using both the ground-truth parameter set and the inferred parameter sets obtained from both low and high displacement measurement noise-affected heterogeneous training experiments. The correlation between the strain energy predicted by the inferred parameter sets Ψ and the ground truth Ψ^{GT} is shown as a hexbin plot in Figure 13. The black diagonal centerline indicates optimal behavior, i.e. the inferred mechanical response matches the expected ground-truth response perfectly. In line with our prior results for the weakest identifiability of the noise-affected *circ-long-het* specimen in the parameter inference and uni-modal stress inference analysis, this specimen also yields the lowest strain-energy agreement across the multi-modal deformation modes with $R^2 = 0.91$ in the low-noise setting and $R^2 = 0.931$ in the high-noise setting. Across the three heterogeneous slabs

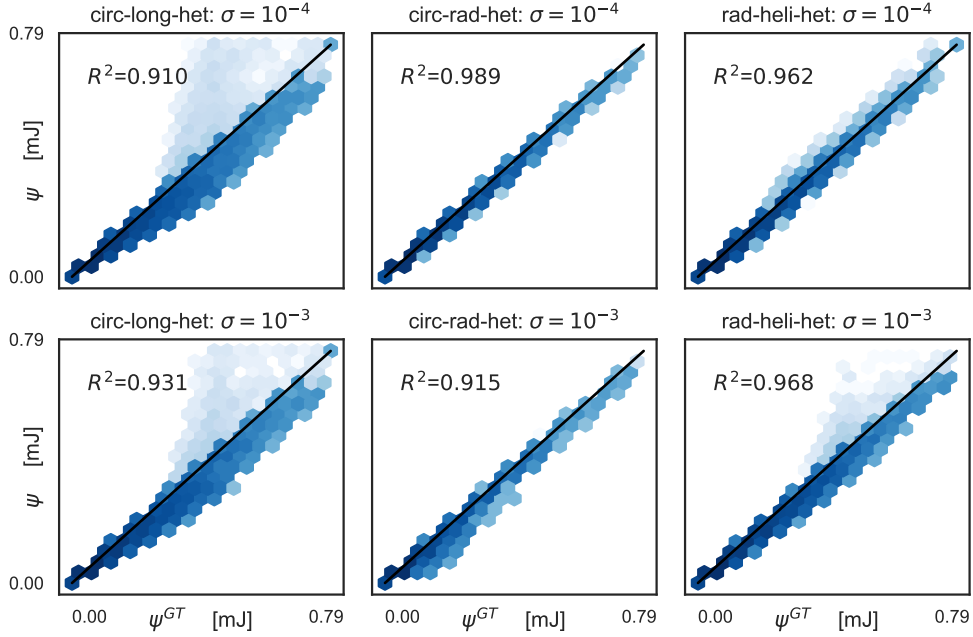


Figure 13: **Strain-energy generalization under mixed-modal deformations.** Correlation between strain energy predicted by inferred parameter posteriors, Ψ , and the ground-truth strain energy, Ψ^{GT} , over 5,000 accepted mixed-modal deformation states sampled in invariant space (Figure 12). Results are shown for geometrically heterogeneous training specimens under both low and high displacement measurement noise, i.e. $\sigma_u = 10^{-4}$ and 10^{-3} mm respectively. Hexbin density emphasizes the dominant response region, and the black diagonal indicates perfect agreement. Despite noise-driven degradation of select parameter groups, predicted energies remain strongly correlated with the ground-truth across mixed-modal states (all $R^2 \geq 0.9$).

tested, we observe larger deviations away from the diagonal, indicating that a subset of randomly sampled invariant combinations, together with corresponding posterior samples, lead to strain energies that differ more strongly from the ground-truth. The *circ-rad-het* specimen shows a very high coefficient of determination in the low-noise case ($R^2 = 0.989$), and its performance slightly degrades to $R^2 = 0.915$ in the high-noise case. Despite this drop, *circ-rad-het* exhibits the tightest clustering of hexbin intensities around the diagonal, suggesting that most mixed-modal states are still well captured, with a relatively small number of outliers contributing to the R^2 reduction. Lastly, the most consistent performing sample is the *rad-heli-het* with an R^2 score of 0.962 in the low noise setting and 0.968 in the high noise setting.

Overall, the mixed-modal strain-energy validation indicates that, even though high displacement noise can substantially perturb individual parameter estimates—particularly the shear-coupling and some directional anisotropic terms—the inferred models retain strong predictive capability at the level of strain energy across a broad set of physiologically admissible deformation states (all $R^2 \geq 0.9$). This finding complements the stress-based validation and suggests that the proposed single-shot full-field identification framework can generalize reliably beyond the specific training protocol, provided that geometric and microstructural heterogeneity are sufficiently rich and measurement noise remains within a moderate range.

6. Discussion

The ability to infer complex orthotropic hyperelastic models from a single full-field biaxial tensile testing experiment represents an interesting avenue in biomechanical tissue characterization. Conventional constitutive identification workflows for complex orthotropic tissues, such as the heart muscle, typically rely on assumed microstructural homogeneity across the tissue specimen and leverage multiple specialized uni-modal loading protocols to identify constitutive parameter sets [10, 11, 74]. This reflects a broader challenge for orthotropic HO myocardium laws: parameter

uniqueness is generally difficult to guarantee under limited excitation, motivating multi-modal protocols, sensitivity-informed reparameterizations, or model reduction [15, 75, 76, 77] This work demonstrates that a single heterogeneous biaxial experiment, when combined with full-field kinematics and sparse reaction-force measurements, can support uncertainty-aware inference of a nonlinear orthotropic Holzapfel–Ogden (HO) parameter set using stochastic variational inference. Beyond the identifiability perspective, this single-shot strategy reduces experimental tissue manipulation and is particularly attractive for heterogeneous biological tissues, where sample availability or repeat testing is limited. Across the considered slab configurations, two consistent findings emerge: (i) identifiability is primarily governed by the degree to which the experiment excites the relevant invariant subspace, and (ii) even when individual HO parameters are not recovered accurately under varying levels of displacement measurement noise, the inferred models can remain highly predictive for stresses and strain energy over both uni-modal and mixed-modal deformation states. These observations clarify when single-shot full-field inference can be expected to recover the full parameter set, and when it should instead be interpreted as delivering a reliable posterior predictive constitutive response with quantified uncertainty.

Heterogeneity as an experimental design principle for orthotropic constitutive parameter inference. Dominant gains in constitutive parameter identifiability arise from deliberately enriching the deformation space within a single test. Microstructural heterogeneity, introduced through slab orientation inducing specific within-specimen heterogeneity through transmural fiber rotation, and geometric heterogeneity, introduced through a central occlusion, both broaden the activated distributions of I_1 , I_{4ff} , I_{4nn} , and I_{4fs} (Figures 4-5). These microstructural or geometric experimental protocol choices increase the sensitivity of the equilibrium residuals to the full parameter vector θ . In the noise-free setting, this explains the contrast between homogeneous and heterogeneous specimens in Figures 6-7. Most isotropic and primary anisotropic parameters are inferred robustly across configurations, while the shear-coupling parameters (a_{fs}, b_{fs}) become practically identifiable only when the single slab biaxial tension experiment produces appreciable I_{4fs} excitation. The *circ-rad-het* and *rad-heli-het* slab configurations provide the most consistent recovery of these terms, reflecting the combined effect of geometry-induced strain gradients and orientation-driven multiaxial activation of the microstructure. In this sense, our results translate the multi-modal calibration message from prior myocardium studies into a single-shot setting: rather than combining separate stretch and shear protocols, we aim to excite the same (otherwise weakly constrained) coupling modes within one heterogeneous experiment [10, 11, 15]. These results further suggest that future protocols could deliberately combine geometrical and microstructural tailoring to maximize parameter observability within a single specimen.

Experimental displacement measurement noise selectively impacts constitutive parameter identifiability. Displacement noise degrades constitutive parameter identifiability selectively rather than uniformly. For low noise ($\sigma_u = 10^{-4}$ mm), Figures 8-9 show stable convergence and comparatively narrow posteriors for the isotropic and primary anisotropic parameters. In contrast, (a_{fs}, b_{fs}) shows the largest posterior broadening and, in some cases, pronounced skewness or truncation of the inferred posterior parameter distribution. For high noise ($\sigma_u = 10^{-3}$ mm), the shear-coupling terms lose practical identifiability across specimens, and additional degradation can appear in directional anisotropic parameters, most clearly in *circ-rad-het*. These results are consistent with global sensitivity and inverse uncertainty quantification studies of the underlying Holzapfel-Ogden constitutive model [43, 77, 78], which show that parameter sensitivity and practical identifiability depend strongly on the deformation modes and invariant support represented in the available data. Two implications follow. Full-field single-shot inference strongly benefits from experimental designs that amplify invariants associated with weaker energy modes. In addition, posterior-shape diagnostics such as truncation and skewness provide useful indicators of noise-driven practical non-identifiability and should be interpreted alongside point estimates.

Identifiability versus predictive capability: how important is it to identify all the underlying constitutive parameters. An important result is that imperfect recovery of ground-truth HO parameters does not necessarily imply poor constitutive prediction, as also noted in prior HO calibration and in vivo estimation studies [75]. Figures 10-11 show that posterior predictive stresses under classical homogeneous uni-modal protocols remain accurate in aggregate, even at high noise. Figure 13 shows strong strain-energy correlation across 5,000 physiologically admissible mixed-modal deformation states, with all $R^2 \geq 0.9$. When viewed together with the parameter-level degradation in Figures 8-9, these results indicate that distinct parameter combinations can yield near-indistinguishable macroscopic responses over the rich explored invariant deformation space [15, 77] In such cases, the posterior predictive response, together

with its credible interval becomes more relevant for downstream simulation than any single best-fit parameter vector and is consistent with inference perspectives that emphasize parameter ranges rather than unique point estimates. This perspective is particularly pertinent for soft tissues, where measurement noise, limited loading diversity, and intrinsic variability constrain practical identifiability.

Some heterogeneous configurations remain more predictive under noise. Our validation results also reveal slab-specific trends. The *circ-rad-het* configuration can be more sensitive to displacement noise in the uni-modal and mixed-modal validations, despite exhibiting a rich heterogeneous deformation profile in Figure 5. This observation indicates that heterogeneity alone is not sufficient. Identifiability also depends on how displacement measurement noise perturbs the invariants that control weaker energy modes and how these perturbations propagate through the equilibrium residuals, which is consistent with the broader observation that the subset of HO terms supported by data depends on the deformation modes represented in the calibration dataset [15]. In contrast, *rad-heli-het* exhibits the most consistent predictive performance across stress and energy validations in Figures 10-13, making it a promising slicing orientation when a single-shot protocol is prioritized and robust in-plane excitation of multiple microstructural constituent contributions is feasible.

Outlook. Some limitations motivate future work. The results are obtained on synthetic data with known boundary conditions, known microstructural fields, and an assumed HO model form. Future experimental work will need to address boundary-condition uncertainty, microstructure dispersion error or misregistration, and model discrepancy [79, 80]. More broadly, automated model discovery frameworks provide an interesting avenue to deal with both practical non-identifiability and model-form discrepancy in settings with complex loading patterns and varying amounts of measurement noise [16, 30, 32, 33, 53, 81]. Complementary directions include explicit probabilistic models for displacement measurement error, experimental designs that target weakly activated invariants, and alternative variational weighting strategies to improve robustness under noisy full-field data [29, 73, 82]. Variational families that capture posterior dependencies more accurately, combined with posterior predictive checks tailored to equilibrium residuals, would further strengthen uncertainty quantification. Finally, the present study focused on spatially homogeneous material parameters with spatially varying structure fields. Extending the framework to spatially varying parameter fields with appropriate regularization could be valuable for truly heterogeneous tissues, while raising additional identifiability and experimental design challenges [83, 84].

Overall, our results support single-shot, uncertainty-aware identification of nonlinear orthotropic constitutive behavior from a single heterogeneous biaxial test. Our main experimental design message is that the relevant invariant subspace must be sufficiently activated, with particular emphasis on the weak shear-coupling mode. At the same time, the validation results show that posterior predictive accuracy can remain high even when individual parameters are noise-limited.

7. Conclusion

We presented a physics-informed stochastic variational framework that recovers the full constitutive parameter set of a nonlinear orthotropic hyperelastic model from a single biaxial stretch experiment. By exploiting intrinsic microstructural heterogeneity, or introducing simple geometric heterogeneity when needed, the method identifies not only the dominant tensile parameters but also shear-coupling terms that are typically weakly excited in biaxial tension. Our results demonstrate that an effective balance between underlying microstructure and biaxial loading improves identifiability, and that this balance can be set through slicing and tissue harvesting. Circumferential–radial slabs and rotated cuts that place both fiber and sheet directions in the loading plane enable recovery of the full parameter set under noise-free conditions. Under realistic displacement measurement noise, the approach remains robust and yields stresses and strain energies in close agreement with the ground-truth mechanical response, while providing posterior uncertainty estimates for parameters and predicted stresses and strain energies. Adding geometric heterogeneity, a central occlusion for example, systematically improves convergence and tightens posterior distributions, particularly for shear-related parameters. These results indicate that slicing protocols and experimental design can be used deliberately to enhance observability in full-field inverse characterization. More broadly, the framework enables localized characterization of orthotropic nonlinear biological tissues from a single heterogeneous full-field experiment. The pro-

posed framework therefore provides a practical route to single-shot, uncertainty-aware constitutive characterization that is compatible with emerging full-field experimental modalities. This reduces experimental tissue manipulation, improves reproducibility, and supports studies where available tissue is limited.

Acknowledgements

M.P. acknowledges support through the NWO Veni Talent Award 20058.

References

- [1] M. Peirlinck, F. S. Costabal, J. Yao, J. M. Guccione, S. Tripathy, Y. Wang, D. Ozturk, P. Segars, T. M. Morrison, S. Levine, E. Kuhl, Precision medicine in human heart modeling: Perspectives, challenges, and opportunities, *Biomechanics and Modeling in Mechanobiology* 20 (3) (2021) 803–831. doi:10.1007/s10237-021-01421-z.
- [2] S. A. Niederer, K. S. Campbell, S. G. Campbell, A short history of the development of mathematical models of cardiac mechanics, *Journal of Molecular and Cellular Cardiology* (2019). doi:10.1016/j.yjmcc.2018.11.015.
- [3] C. Reeps, A. Maier, J. Pelisek, F. Härtl, V. Grabher-Meier, W. A. Wall, M. Essler, H.-H. Eckstein, M. W. Gee, Measuring and modeling patient-specific distributions of material properties in abdominal aortic aneurysm wall, *Biomechanics and Modeling in Mechanobiology* 12 (4) (2012) 717–733. doi:10.1007/s10237-012-0436-1.
- [4] S. Roccabianca, C. A. Figueroa, G. Tellides, J. D. Humphrey, Quantification of regional differences in aortic stiffness in the aging human, *Journal of the Mechanical Behavior of Biomedical Materials* 29 (2014) 618–634. doi:10.1016/j.jmbbm.2013.01.026.
- [5] S. Budday, G. Sommer, C. Birkel, C. Langkammer, J. Haybaeck, J. Kohnert, M. Bauer, F. Paulsen, P. Steinmann, E. Kuhl, G. A. Holzapfel, Mechanical characterization of human brain tissue, *Acta Biomaterialia* 48 (2017) 319–340. doi:10.1016/j.actbio.2016.10.036.
- [6] K. Matouš, M. G. D. Geers, V. G. Kouznetsova, A. Gillman, A review of predictive nonlinear theories for multiscale modeling of heterogeneous materials, *Journal of Computational Physics* 330 (2017) 192–220. doi:10.1016/j.jcp.2016.10.070.
- [7] N. Famaey, H. Fehervary, Y. Lafon, A. Akyildiz, S. Dreesen, K. Bruyère-Garnier, J.-M. Allain, M. Alloisio, A. Aparici-Gil, C. Catalano, F. Chassagne, S. Chokhandre, K. Crevits, H. Crielaard, E. Cunnane, C. Cunnane, K. De Leener, A. Desai, R. Driessen, A. Erdemir, M. Eskandari, S. Evans, C. Gasser, M. Gebhardt, B. Glas-macher, G. A. Holzapfel, M. Isasi, L. Jennings, S. Kurz, S. Leal-Marín, P. Lecomte, A. Morch, J. Mulvihill, F. Nemavhola, T. Pandelani, S. Pasta, E. Peña, B. Pierrat, H.-L. Ploeg, S. Polzer, M. Rausch, D. Schwarz, H. Screen, S. Sherifova, G. Sommer, S. Wang, D. Walsh, D. Yadav, T. Marchal, L. Geris, Community challenge towards consensus on characterization of biological tissue: C4bio’s first findings, *Journal of Biomechanics* (2026). doi:10.1016/j.jbiomech.2025.113021.
- [8] D. Rohmer, A. Sitek, G. T. Gullberg, Reconstruction and Visualization of Fiber and Laminar Structure in the Normal Human Heart from Ex Vivo Diffusion Tensor Magnetic Resonance Imaging (DTMRI) Data, *Investigative Radiology* 42 (11) (2007) 777. doi:10.1097/RLI.0b013e3181238330.
- [9] D. B. E. Alexander J. Wilson, Myocardial mesostructure and mesofunction (Mar. 2022). doi:10.1152/ajpheart.00059.2022.
- [10] S. Dokos, B. H. Smaill, A. A. Young, I. J. LeGrice, Shear properties of passive ventricular myocardium, *American Journal of Physiology-Heart and Circulatory Physiology* 283 (6) (2002) H2650–H2659. doi:10.1152/ajpheart.00111.2002.

- [11] G. Sommer, A. J. Schriefl, M. Andrä, M. Sacherer, C. Viertler, H. Wolinski, G. A. Holzapfel, Biomechanical properties and microstructure of human ventricular myocardium, *Acta Biomaterialia* 24 (2015) 172–192. doi:10.1016/j.actbio.2015.06.031.
- [12] S. Kakaletsis, W. D. Meador, M. Mathur, G. P. Sugerman, T. Jazwiec, M. Malinowski, E. Lejeune, T. A. Timek, M. K. Rausch, Right ventricular myocardial mechanics: Multi-modal deformation, microstructure, modeling, and comparison to the left ventricle, *Acta Biomaterialia* 123 (2021) 154–166. doi:10.1016/j.actbio.2020.12.006.
- [13] B. Staber, J. Guilleminot, Stochastic hyperelastic constitutive laws and identification procedure for soft biological tissues with intrinsic variability, *Journal of the Mechanical Behavior of Biomedical Materials* 65 (2017) 743–752. doi:10.1016/j.jmbbm.2016.09.022.
- [14] G. A. Holzapfel, R. W. Ogden, Constitutive modelling of passive myocardium: a structurally based framework for material characterization, *Philosophical Transactions of the Royal Society A: Mathematical, Physical and Engineering Sciences* 367 (1902) (2009) 3445–3475. doi:10.1098/rsta.2009.0091.
- [15] D. Guan, F. Ahmad, P. Theobald, S. Soe, X. Luo, H. Gao, On the aic-based model reduction for the general holzapfel–ogden myocardial constitutive law, *Biomechanics and Modeling in Mechanobiology* 18 (4) (2018) 1213–1232. doi:10.1007/s10237-019-01140-6.
- [16] D. Martonová, M. Peirlinck, K. Linka, G. A. Holzapfel, S. Leyendecker, E. Kuhl, Automated model discovery for human cardiac tissue: Discovering the best model and parameters, *Computer Methods in Applied Mechanics and Engineering* 428 (2024) 117078. doi:10.1016/j.cma.2024.117078.
- [17] H. Fehervary, M. Smoljkić, J. Vander Sloten, N. Famaey, Planar biaxial testing of soft biological tissues, Ph.D. thesis, KU Leuven (2018).
- [18] M. Alloisio, J. J. M. Wolffs, T. C. Gasser, Specimen width affects vascular tissue integrity for in-vitro characterisation, *Journal of the Mechanical Behavior of Biomedical Materials* 154 (2024) 106520. doi:10.1016/j.jmbbm.2024.106520.
- [19] T. Vervenne, N. Vermeeren, N. Demeersseman, H. Fehervary, M. Peirlinck, E. Kuhl, N. Famaey, Stretching the limits: From planar-biaxial stress–stretch to arterial pressure–diameter, *Journal of Biomechanical Engineering* (2026). doi:10.1115/1.4070124.
- [20] Z. Wang, J. B. Estrada, E. M. Arruda, K. Garikipati, Inference of deformation mechanisms and constitutive response of soft material surrogates of biological tissue by full-field characterization and data-driven variational system identification, *Journal of the Mechanics and Physics of Solids* 153 (2021) 104474. doi:10.1016/j.jmps.2021.104474.
- [21] C. Jailin, A. Benady, R. Legroux, E. Baranger, Experimental learning of a hyperelastic behavior with a physics-augmented neural network, *Experimental Mechanics* 64 (9) (2024) 1465–1481. doi:10.1007/s11340-024-01106-5.
- [22] S. Meng, A. A. K. Yousefi, S. Avril, Machine-learning-based virtual fields method: Application to anisotropic hyperelasticity, *Computer Methods in Applied Mechanics and Engineering* 434 (2025) 117580. doi:10.1016/j.cma.2024.117580.
- [23] M. Grédiac, F. Pierron, S. Avril, E. Toussaint, The virtual fields method for extracting constitutive parameters from full-field measurements: a review, *Strain* 42 (4) (2006) 233–253. doi:10.1111/j.1475-1305.2006.tb01504.x.
- [24] F. Pierron, M. Grédiac, *The Virtual Fields Method: Extracting Constitutive Mechanical Parameters from Full-field Deformation Measurements*, Springer New York, 2012. doi:10.1007/978-1-4614-1824-5.

- [25] K. T. Kavanagh, R. W. Clough, Finite element applications in the characterization of elastic solids, *International Journal of Solids and Structures* 7 (1) (1971) 11–23. doi:10.1016/0020-7683(71)90015-1.
- [26] M. Peirlinck, K. L. Sack, P. De Backer, P. Morais, P. Segers, T. Franz, M. De Beule, Kinematic boundary conditions substantially impact in silico ventricular function, *International Journal for Numerical Methods in Biomedical Engineering* 35 (1) (Oct. 2018). doi:10.1002/cmm.3151.
- [27] A. Elouneq, D. Sutula, J. Chambert, A. Lejeune, S. P. A. Bordas, E. Jacquet, An open-source fenics-based framework for hyperelastic parameter estimation from noisy full-field data: Application to heterogeneous soft tissues, *Computers & Structures* 255 (2021) 106620. doi:10.1016/j.compstruc.2021.106620.
- [28] D. Claire, F. Hild, S. Roux, A finite element formulation to identify damage fields: the equilibrium gap method, *International Journal for Numerical Methods in Engineering* 61 (2) (2004) 189–208. doi:10.1002/nme.1057.
- [29] A. Peyraut, M. Genet, Finite strain formulation of the discrete equilibrium gap principle: application to direct parameter estimation from large full-fields measurements, *Comptes Rendus. Mécanique* 353 (G1) (2025) 259–309. doi:10.5802/crmeca.279.
- [30] M. Flaschel, S. Kumar, L. De Lorenzis, Unsupervised discovery of interpretable hyperelastic constitutive laws, *Computer Methods in Applied Mechanics and Engineering* 381 (2021) 113852. doi:10.1016/j.cma.2021.113852.
- [31] P. Thakolkaran, A. Joshi, Y. Zheng, M. Flaschel, L. De Lorenzis, S. Kumar, NN-EUCLID: Deep-learning hyperelasticity without stress data, *Journal of the Mechanics and Physics of Solids* 169 (July) (2022) 105076. doi:10.1016/j.jmps.2022.105076.
- [32] A. Joshi, P. Thakolkaran, Y. Zheng, M. Escande, M. Flaschel, L. De Lorenzis, S. Kumar, Bayesian-euclid: Discovering hyperelastic material laws with uncertainties, *Computer Methods in Applied Mechanics and Engineering* 398 (2022) 115225. doi:10.1016/j.cma.2022.115225.
- [33] P. Thakolkaran, Y. Guo, S. Saini, M. Peirlinck, B. Alheit, S. Kumar, Can kan cans? input-convex kolmogorov-arnold networks (kans) as hyperelastic constitutive artificial neural networks (cans) (2025). doi:10.48550/ARXIV.2503.05617.
- [34] S. NIELLES-VALLESPIN, Z. Khalique, P. F. Ferreira, R. de Silva, A. D. Scott, P. Kilner, L.-A. McGill, A. Giannakidis, P. D. Gatehouse, D. Ennis, E. Aliotta, M. Al-Khalil, P. Kellman, D. Mazilu, R. S. Balaban, D. N. Firmin, A. E. Arai, D. J. Pennell, Assessment of Myocardial Microstructural Dynamics by In Vivo Diffusion Tensor Cardiac Magnetic Resonance, *Journal of the American College of Cardiology* 69 (6) (2017) 661–676. doi:10.1016/j.jacc.2016.11.051.
- [35] P. Hauseux, J. S. Hale, S. Cotin, S. P. A. Bordas, Quantifying the uncertainty in a hyperelastic soft tissue model with stochastic parameters, *Applied Mathematical Modelling* 62 (2018) 86–102. doi:10.1016/j.apm.2018.04.021.
- [36] D. Ozturk, S. Kotha, S. Ghosh, An uncertainty quantification framework for multiscale parametrically homogenized constitutive models (phcms) of polycrystalline ti alloys, *Journal of the Mechanics and Physics of Solids* 148 (2021) 104294. doi:10.1016/j.jmps.2021.104294.
- [37] A. Aggarwal, B. S. Jensen, S. Pant, C.-H. Lee, Strain energy density as a gaussian process and its utilization in stochastic finite element analysis: Application to planar soft tissues, *Computer Methods in Applied Mechanics and Engineering* 404 (2023) 115812. doi:10.1016/j.cma.2022.115812.
- [38] A. Peshave, F. Pierron, P. Lava, D. Moens, D. Vandepitte, Practical Uncertainty Quantification Guidelines for DIC-Based Numerical Model Validation, *Experimental Techniques* (Oct. 2024). doi:10.1007/s40799-024-00758-1.

- [39] D. Anton, J.-A. Tröger, H. Wessels, U. Römer, A. Henkes, S. Hartmann, Deterministic and statistical calibration of constitutive models from full-field data with parametric physics-informed neural networks (2024). doi: [10.48550/ARXIV.2405.18311](https://doi.org/10.48550/ARXIV.2405.18311).
- [40] V. Taç, M. K. Rausch, I. Billionis, F. Sahli Costabal, A. B. Tepole, Generative hyperelasticity with physics-informed probabilistic diffusion fields, *Engineering with Computers* 41 (1) (2024) 51–69. doi: [10.1007/s00366-024-01984-2](https://doi.org/10.1007/s00366-024-01984-2).
- [41] K. Linka, G. A. Holzapfel, E. Kuhl, Discovering uncertainty: Bayesian constitutive artificial neural networks, *Computer Methods in Applied Mechanics and Engineering* 433 (2025) 117517. doi: [10.1016/j.cma.2024.117517](https://doi.org/10.1016/j.cma.2024.117517).
- [42] K. D. Costa, J. W. Holmes, A. D. McCulloch, Modelling cardiac mechanical properties in three dimensions, *Philosophical Transactions of the Royal Society of London. Series A: Mathematical, Physical and Engineering Sciences* 359 (1783) (2001) 1233–1250. doi: [10.1098/rsta.2001.0828](https://doi.org/10.1098/rsta.2001.0828).
- [43] N. Laita, M. Á. Martínez, M. Doblaré, E. Peña, On the myocardium modeling under multimodal deformations: a comparison between costa’s, holzapfel and ogden’s formulations, *Meccanica* (Apr. 2025). doi: [10.1007/s11012-025-01959-7](https://doi.org/10.1007/s11012-025-01959-7).
- [44] R. Avazmohammadi, J. S. Soares, D. S. Li, S. S. Raut, R. C. Gorman, M. S. Sacks, A Contemporary Look at Biomechanical Models of Myocardium, *Annual Review of Biomedical Engineering* 21 (2019) 417–442. doi: [10.1146/annurev-bioeng-062117-121129](https://doi.org/10.1146/annurev-bioeng-062117-121129).
- [45] X. Navy, Z. Sheng, K. Kim, J. M. Cormack, Three-dimensional tissue strain measurement using a row–column array during biaxial testing of excised ventricular porcine myocardium, *Ultrasound in Medicine & Biology* 51 (9) (2025) 1622–1626. doi: <https://doi.org/10.1016/j.ultrasmedbio.2025.05.007>.
- [46] J. B. Estrada, C. M. Luetkemeyer, U. M. Scheven, E. M. Arruda, MR-u: Material Characterization Using 3D Displacement-Encoded Magnetic Resonance and the Virtual Fields Method, *Experimental Mechanics* 60 (7) (2020) 907–924. doi: [10.1007/s11340-020-00595-4](https://doi.org/10.1007/s11340-020-00595-4).
- [47] S. Davis, A. Karali, T. Balcaen, J. Zekonyte, M. Pétré, M. Roldo, G. Kerckhofs, G. Blunn, Comparison of two contrast-enhancing staining agents for use in x-ray imaging and digital volume correlation measurements across the cartilage-bone interface, *Journal of the Mechanical Behavior of Biomedical Materials* 152 (2024) 106414. doi: <https://doi.org/10.1016/j.jmbbm.2024.106414>.
- [48] R. Alberini, A. Spagnoli, M. J. Sadeghinia, B. Skallerud, M. Terzano, G. A. Holzapfel, Second harmonic generation microscopy, biaxial mechanical tests and fiber dispersion models in human skin biomechanics, *Acta Biomaterialia* 185 (2024) 266–280. doi: [10.1016/j.actbio.2024.07.026](https://doi.org/10.1016/j.actbio.2024.07.026).
- [49] A. Maes, C. Pestiaux, A. Marino, T. Balcaen, L. Leysens, S. Vangrunderbeeck, G. Pyka, W. M. De Borggraeve, L. Bertrand, C. Beauloye, S. Horman, M. Wevers, G. Kerckhofs, Cryogenic contrast-enhanced microCT enables nondestructive 3d quantitative histopathology of soft biological tissues, *Nature Communications* 13 (1) (Oct. 2022). doi: [10.1038/s41467-022-34048-4](https://doi.org/10.1038/s41467-022-34048-4).
- [50] M. Planck, *Vorlesungen über Thermodynamik*, von dr. Max Planck, Veit & Comp., 1897.
- [51] B. D. Coleman, W. Noll, On the thermostatics of continuous media, *Archive for Rational Mechanics and Analysis* 4 (1) (1959) 97–128. doi: [10.1007/BF00281381](https://doi.org/10.1007/BF00281381).
- [52] M. Peirlinck, J. A. Hurtado, M. K. Rausch, A. B. Tepole, E. Kuhl, A universal material model subroutine for soft matter systems, *Engineering with Computers* (Sep. 2024). doi: [10.1007/s00366-024-02031-w](https://doi.org/10.1007/s00366-024-02031-w).
- [53] R. V. Thorat, M. Anas, R. Nayek, S. Chatterjee, System identification and reliability assessment of hyperelastic materials via an efficient sparsity-promoting variational Bayesian approach, *Probabilistic Engineering Mechanics* 80 (2025) 103763. doi: [10.1016/j.probingmech.2025.103763](https://doi.org/10.1016/j.probingmech.2025.103763).

- [54] M. Peirlinck, F. Sahli Costabal, K. L. Sack, J. S. Choy, G. S. Kassab, J. M. Guccione, M. De Beule, P. Segers, E. Kuhl, Using machine learning to characterize heart failure across the scales, *Biomechanics and Modeling in Mechanobiology* 18 (6) (2019) 1987–2001. doi:10.1007/s10237-019-01190-w.
- [55] F. Rodrigues, Scaling bayesian inference of mixed multinomial logit models to large datasets, *Transportation Research Part B: Methodological* 158 (Apr. 2022). doi:10.1016/j.trb.2022.01.005.
- [56] G. Parisi, *Statistical field theory*, Redwood City, CA. : Addison-Wesley Pub. Co., 1988.
- [57] G. Consonni, J. Marin, Mean-field variational approximate bayesian inference for latent variable models, *Computational Statistics & Data Analysis* 52 (Oct. 2007). doi:10.1016/j.csda.2006.10.028.
- [58] S. Kullback, *Information theory and statistics*, New York : Dover Publications, 1968.
- [59] J. A. Cover T., *Information theory and statistics*, Wiley-Interscience, 1968.
- [60] D. Phan, N. Pradhan, M. Jankowiak, Composable Effects for Flexible and Accelerated Probabilistic Programming in NumPyro (Dec. 2019). doi:10.48550/arXiv.1912.11554.
- [61] D. P. Kingma, J. Ba, Adam: A Method for Stochastic Optimization (Jan. 2017).
- [62] D. P. Kingma, M. Welling, Auto-encoding variational bayes (2013). doi:10.48550/ARXIV.1312.6114.
- [63] H. Lombaert, J. Peyrat, P. Croisille, S. Rapacchi, L. Fanton, F. Cheriet, P. Clarysse, I. Magnin, H. Delingette, N. Ayache, Human atlas of the cardiac fiber architecture: Study on a healthy population, *IEEE Transactions on Medical Imaging* 31 (7) (2012) 1436–1447. doi:10.1109/tmi.2012.2192743.
- [64] Dassault Systèmes Simulia Corp., *Abaqus Analysis User’s guide*, Dassault Systèmes Simulia Corp., Providence, RI, USA, 2025.
- [65] P. J. Flory, Thermodynamic relations for high elastic materials, *Transactions of the Faraday Society* 57 (1961) 829. doi:10.1039/tf9615700829.
- [66] A. J. M. Spencer, *Constitutive Theory for Strongly Anisotropic Solids*, Springer Vienna, 1984, pp. 1–32. doi:10.1007/978-3-7091-4336-0_1.
- [67] A. Menzel, Modelling of anisotropic growth in biological tissues: A new approach and computational aspects, *Biomechanics and Modeling in Mechanobiology* 3 (3) (2004) 147–171. doi:10.1007/s10237-004-0047-6.
- [68] W. H. Wittrick, A generalization of macaulay’s method with applications in structural mechanics, *AIAA Journal* 3 (2) (1965) 326–330. doi:10.2514/3.2849.
- [69] P. Wriggers, J. Schröder, F. Auricchio, Finite element formulations for large strain anisotropic material with inextensible fibers, *Advanced Modeling and Simulation in Engineering Sciences* 3 (1) (2016) 25. doi:10.1186/s40323-016-0079-3.
- [70] E. McEvoy, G. A. Holzapfel, P. McGarry, Compressibility and Anisotropy of the Ventricular Myocardium: Experimental Analysis and Microstructural Modeling, *Journal of Biomechanical Engineering* 140 (8) (May 2018). doi:10.1115/1.4039947.
- [71] F. C. Yin, C. C. Chan, R. M. Judd, Compressibility of perfused passive myocardium, *American Journal of Physiology-Heart and Circulatory Physiology* 271 (5) (1996) H1864–H1870. doi:10.1152/ajpheart.1996.271.5.H1864.
- [72] B. Rahmani, F. Mortazavi, I. Villemure, M. Levesque, A new approach to inverse identification of mechanical properties of composite materials: Regularized model updating, *Composite Structures* 105 (2013) 116–125. doi:10.1016/j.compstruct.2013.04.025.

- [73] A. Jafari, K. Vlachas, E. Chatzi, J. F. Unger, A Bayesian framework for constitutive model identification via use of full field measurements, with application to heterogeneous materials, *Computer Methods in Applied Mechanics and Engineering* 433 (2025) 117489. doi:10.1016/j.cma.2024.117489.
- [74] R. Avazmohammadi, D. S. Li, T. Leahy, E. Shih, J. S. Soares, J. H. Gorman, R. C. Gorman, M. S. Sacks, An integrated inverse model-experimental approach to determine soft tissue three-dimensional constitutive parameters: application to post-infarcted myocardium, *Biomechanics and Modeling in Mechanobiology* 17 (1) (2018) 31–53. doi:10.1007/s10237-017-0943-1.
- [75] H. Gao, W. G. Li, L. Cai, C. Berry, X. Y. Luo, Parameter estimation in a holzapfel–ogden law for healthy myocardium, *Journal of Engineering Mathematics* (2015). doi:10.1007/s10665-014-9740-3.
- [76] A. Palit, S. K. Bhudia, T. N. Arvanitis, G. A. Turley, M. A. Williams, In vivo estimation of passive biomechanical properties of human myocardium, *Medical & Biological Engineering & Computing* (2018). doi:10.1007/s11517-017-1768-x.
- [77] A. Lazarus, D. Dalton, D. Husmeier, H. Gao, Sensitivity analysis and inverse uncertainty quantification for the left ventricular passive mechanics, *Biomechanics and Modeling in Mechanobiology* (2022). doi:10.1007/s10237-022-01571-8.
- [78] G. Balaban, M. S. Alnæs, J. Sundnes, M. E. Rognes, Adjoint multi-start-based estimation of cardiac hyperelastic material parameters using shear data, *Biomechanics and Modeling in Mechanobiology* (2016). doi:10.1007/s10237-016-0780-7.
- [79] D. Martonová, S. Leyendecker, G. A. Holzapfel, E. Kuhl, Discovering dispersion: How robust is automated model discovery for human myocardial tissue?, *Biomechanics and Modeling in Mechanobiology* (2025). doi:10.1007/s10237-025-02005-x.
- [80] J. Vaverka, J. Burša, A modification of holzapfel–ogden hyperelastic model of myocardium better describing its passive mechanical behavior, *European Journal of Mechanics - A/Solids* (2025). doi:10.1016/j.euromechsol.2025.105586.
- [81] K. Linka, E. Kuhl, A new family of Constitutive Artificial Neural Networks towards automated model discovery, *Computer Methods in Applied Mechanics and Engineering* 403 (2023) 115731. doi:10.1016/j.cma.2022.115731.
- [82] A. Marek, F. M. Davis, M. Rossi, F. Pierron, Extension of the sensitivity-based virtual fields to large deformation anisotropic plasticity, *Int J Mater Form* 12 (3) (2019) 457–476. doi:10.1007/s12289-018-1428-1.
- [83] S. Ghouli, M. Flaschel, S. Kumar, L. De Lorenzis, A topology optimisation framework to design test specimens for one-shot identification or discovery of material models, *Journal of the Mechanics and Physics of Solids* 203 (2025) 106210. doi:10.1016/j.jmps.2025.106210.
- [84] K. L. Chaurasiya, S. Dutta, S. Kumar, A. Joshi, Hetero-euclid: Interpretable model discovery for heterogeneous hyperelastic materials using stress-unsupervised learning (2025). doi:10.48550/ARXIV.2509.11784.
- [85] N. J. Higham, Computing real square roots of a real matrix, *Linear Algebra and its Applications* 88–89 (1987) 405–430. doi:10.1016/0024-3795(87)90118-2.

Appendix A. Tissue slab geometry and loading conditions

We summarize the tissue slab geometry and loading conditions used for synthetic data generation in Figure A.1.

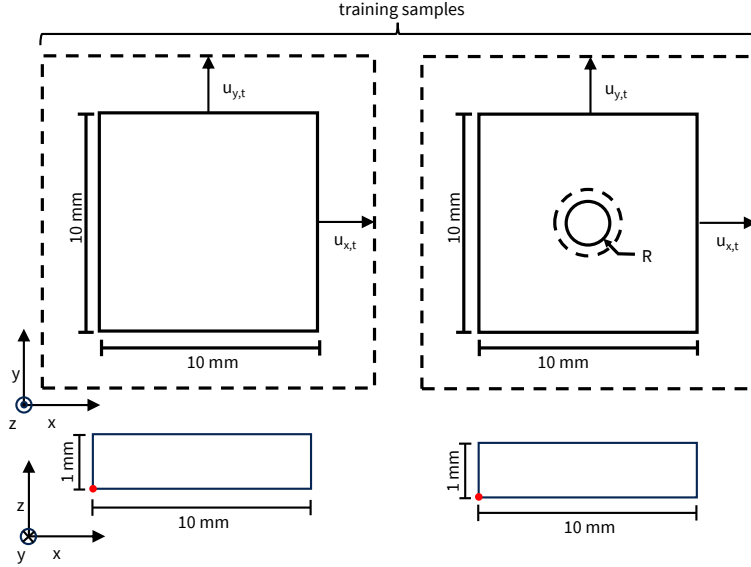


Figure A.1: **Synthetic data generation: training sample dimensions and loading conditions** Tissue slab geometry and applied boundary conditions for the training samples. We subject all training samples to a biaxial loading protocol $\lambda_1 : \lambda_2 - (1 : 2), (1 : 1), (2 : 1)$ up to 15% of the initial length of the sample. All samples are of size $10 \times 10 \times 1 \text{ mm}^3$. The geometrically heterogeneous tissue samples have a circular occlusion in the center with a radius of $R = 1 \text{ mm}$.

Appendix B. Noise-free orthotropic constitutive parameter inference results

This appendix contains the numerical results for the parameter fitting procedure when no displacement noise is applied to the experiments. In Table B.2, we show the optimized hyperparameters at the final epoch. The parameters themselves and their accompanying standard deviation are reported in Table B.3. Finally, we also report the relative error between the estimated material model parameters and the ground-truth in Table B.4.

Table B.2: **Hyperparameter estimates.** The hyperparameters at the final epoch of the optimization procedure for the samples with and without circular occlusion. The hyperparameters are both for inverse-gamma distributions where α_* , β_* are the scale and rate parameters.

	circ-long-hom	circ-rad-hom	rad-heli-hom	circ-long-het	circ-rad-het	rad-heli-het
α_{v_s}	1.914×10^1	1.928×10^1	1.928×10^1	1.916×10^1	1.930×10^1	1.930×10^1
α_σ	5.215×10^6	5.050×10^6	5.101×10^6	5.400×10^6	5.127×10^6	5.292×10^6
β_{v_s}	7.401×10^7	7.201×10^7	7.169×10^7	7.924×10^7	7.720×10^7	7.714×10^7
β_σ	1.901×10^1	1.836×10^1	1.854×10^1	1.834×10^1	1.733×10^1	1.789×10^1

Table B.3: **Parameter estimates.** The parameters at the final epoch of the optimization procedure for the samples with and without circular occlusion. Parameters in θ are written out in full to correspond to the HO-model parameters. The corresponding standard deviation has also been reported.

Parameters	circ-long-hom	circ-rad-hom	rad-heli-hom	circ-long-het	circ-rad-het	rad-heli-het
<i>Inferred μ_θ:</i>						
a	8.090×10^{-4}					
b	7.474×10^0					
a_f	1.911×10^{-3}					
b_f	2.206×10^1					
a_n	2.270×10^{-4}					
b_n	3.480×10^1	3.479×10^1	3.480×10^1	3.480×10^1	3.479×10^1	3.480×10^1
a_{fs}	7.806×10^{-2}	5.426×10^{-4}	5.480×10^{-4}	5.414×10^{-4}	5.484×10^{-4}	5.476×10^{-4}
b_{fs}	4.548×10^{-1}	4.715×10^0	3.561×10^0	6.862×10^{-1}	5.700×10^0	5.652×10^0
K	1.000×10^{-1}					
<i>Inferred σ_θ:</i>						
σ_a	1.792×10^{-8}	1.513×10^{-8}	1.518×10^{-8}	1.756×10^{-8}	1.684×10^{-8}	1.600×10^{-8}
σ_b	1.223×10^{-4}	9.733×10^{-5}	9.650×10^{-5}	1.268×10^{-4}	1.064×10^{-4}	1.125×10^{-4}
σ_{a_f}	4.608×10^{-9}	2.851×10^{-8}	2.972×10^{-8}	5.507×10^{-9}	4.784×10^{-8}	2.798×10^{-8}
σ_{b_f}	2.990×10^{-5}	2.072×10^{-4}	2.109×10^{-4}	3.661×10^{-5}	6.346×10^{-4}	2.022×10^{-4}
σ_{a_n}	1.514×10^{-9}	1.100×10^{-7}	8.551×10^{-9}	1.380×10^{-9}	1.084×10^{-7}	8.144×10^{-9}
σ_{b_n}	6.611×10^{-5}	3.699×10^{-2}	4.123×10^{-4}	7.526×10^{-5}	3.117×10^{-2}	3.880×10^{-4}
$\sigma_{a_{fs}}$	1.906×10^0	4.088×10^{-5}	4.207×10^{-5}	6.564×10^{-5}	4.102×10^{-6}	1.034×10^{-5}
$\sigma_{b_{fs}}$	1.370×10^1	4.410×10^0	3.996×10^0	1.283×10^1	4.534×10^{-2}	2.728×10^{-1}
σ_K	2.363×10^{-7}	6.853×10^{-7}	5.688×10^{-7}	2.296×10^{-7}	8.327×10^{-7}	5.612×10^{-7}

Table B.4: **Relative error of the parameter estimates.** The relative error at the final epoch between the parameter values and the ground-truth for samples with and without circular occlusion and various microstructures.

Relative errors	circ-long-hom	circ-rad-hom	rad-heli-hom	circ-long-het	circ-rad-het	rad-heli-het
\hat{e}_a	4.765×10^{-5}	-1.864×10^{-5}	-2.925×10^{-5}	1.832×10^{-5}	-1.644×10^{-5}	-2.593×10^{-5}
\hat{e}_b	-2.298×10^{-6}	-3.659×10^{-5}	-3.854×10^{-5}	1.223×10^{-5}	-2.795×10^{-5}	-3.428×10^{-5}
\hat{e}_{a_f}	-5.495×10^{-5}	-8.243×10^{-5}	-7.541×10^{-5}	-4.184×10^{-5}	-1.356×10^{-5}	-8.322×10^{-5}
\hat{e}_{b_f}	-1.471×10^{-6}	-4.349×10^{-5}	-4.047×10^{-5}	9.769×10^{-6}	8.735×10^{-6}	-3.724×10^{-5}
\hat{e}_{a_n}	9.655×10^{-5}	1.844×10^{-4}	3.895×10^{-5}	7.867×10^{-5}	2.017×10^{-4}	4.702×10^{-5}
\hat{e}_{b_n}	1.290×10^{-5}	2.250×10^{-4}	-5.078×10^{-5}	-1.396×10^{-5}	4.682×10^{-4}	-4.864×10^{-5}
$\hat{e}_{a_{fs}}$	-1.417×10^2	8.050×10^{-3}	-1.901×10^{-3}	1.023×10^{-2}	-2.520×10^{-3}	-1.137×10^{-3}
$\hat{e}_{b_{fs}}$	9.201×10^{-1}	1.716×10^{-1}	3.743×10^{-1}	8.794×10^{-1}	-1.535×10^{-3}	6.900×10^{-3}
\hat{e}_K	2.423×10^{-6}	-2.932×10^{-5}	-4.502×10^{-5}	4.837×10^{-6}	-1.661×10^{-5}	-4.184×10^{-5}

Appendix C. Noise-affected orthotropic constitutive parameter inference results

This appendix contains the numerical results for the parameter fitting procedure when displacement noise is applied to the experiments. In Table C.5, we show the optimized hyperparameters at the final epoch. The parameters themselves and their accompanying standard deviation are reported in Table C.6. Finally, we also report the relative error between the estimated material model parameters and the ground-truth in Table C.7.

Table C.5: **Hyperparameter estimates for noisy experiments.** The hyperparameters at the final epoch of the optimization procedure for the samples with circular occlusion and additive displacement noise at high ($\sigma = 1e-3$) and low ($\sigma = 1e-4$) levels. The hyperparameters are both for inverse-gamma distributions where α_* , β_* are the scale and rate parameters.

	circ-long-het $\sigma_u = 1e^{-4}$	circ-rad-het $\sigma_u = 1e^{-4}$	rad-heli-het $\sigma_u = 1e^{-4}$	circ-long-het $\sigma_u = 1e^{-3}$	circ-rad-het $\sigma_u = 1e^{-3}$	rad-heli-het $\sigma_u = 1e^{-3}$
α_{v_s}	1.922e+01	1.930e+01	1.928e+01	1.922e+01	1.918e+01	1.923e+01
α_σ	2.615e+06	2.678e+06	2.683e+06	8.849e+05	1.047e+06	9.640e+05
β_{v_s}	1.977e+07	2.076e+07	2.479e+07	2.168e+06	1.052e+06	2.585e+06
β_σ	3.598e+01	3.166e+01	3.250e+01	1.079e+02	8.942e+01	9.801e+01

Table C.6: **Noisy parameter estimates.** The parameters at the final epoch of the optimization procedure for the samples with circular occlusion and additive displacement noise at high ($\sigma = 1e-3$) and low ($\sigma = 1e-4$) levels. Parameters in θ are written out in full to correspond to the HO-model parameters. The corresponding standard deviation has also been reported.

Parameters	circ-long-het $\sigma_u = 1e^{-4}$	circ-rad-het $\sigma_u = 1e^{-4}$	rad-heli-het $\sigma_u = 1e^{-4}$	circ-long-het $\sigma_u = 1e^{-3}$	circ-rad-het $\sigma_u = 1e^{-3}$	rad-heli-het $\sigma_u = 1e^{-3}$
<i>Inferred μ_θ:</i>						
a	8.086e-04	8.051e-04	8.054e-04	8.101e-04	9.909e-04	9.237e-04
b	7.475e+00	7.535e+00	7.489e+00	7.823e+00	8.773e+00	7.919e+00
a_f	1.919e-03	1.988e-03	1.946e-03	2.004e-03	3.670e-03	2.041e-03
b_f	2.202e+01	2.134e+01	2.183e+01	2.129e+01	9.790e+00	2.086e+01
a_n	2.259e-04	2.366e-04	2.288e-04	2.325e-04	3.209e-10	2.496e-04
b_n	3.484e+01	3.133e+01	3.479e+01	3.377e+01	1.865e-01	3.404e+01
a_{fs}	1.644e-08	2.590e-04	4.239e-05	1.224e-08	8.290e-09	1.039e-08
b_{fs}	5.301e-01	9.085e+00	2.487e+01	5.017e-01	1.953e-01	1.499e-02
K	1.000e-01	9.952e-02	1.001e-01	9.922e-02	7.003e-02	9.155e-02
<i>Inferred σ_θ:</i>						
σ_a	6.561e-08	5.847e-08	5.717e-08	5.420e-07	3.137e-07	4.306e-07
σ_b	4.958e-04	3.947e-04	4.232e-04	4.235e-03	1.809e-03	2.792e-03
σ_{af}	1.933e-08	1.765e-07	8.679e-08	1.813e-07	1.922e-06	7.681e-07
σ_{bf}	1.254e-04	2.288e-03	6.918e-04	1.026e-03	1.473e-02	5.697e-03
σ_{an}	5.369e-09	3.939e-07	2.461e-08	5.067e-08	5.002e-08	2.214e-07
σ_{bn}	2.759e-04	1.138e-01	1.364e-03	2.398e-03	4.350e+00	1.103e-02
σ_{af_s}	3.926e-06	8.179e-06	6.189e-06	3.030e-06	1.820e-06	2.152e-06
σ_{bf_s}	1.365e+01	1.662e-01	1.076e+00	1.323e+01	4.074e+00	1.253e+01
σ_K	9.586e-07	2.898e-06	2.220e-06	8.185e-06	1.974e-05	1.785e-05

Table C.7: **Relative errors of the noisy parameter estimates.** The relative error at the final epoch between the parameter values and the ground-truth for samples with circular occlusion, additive displacement noise at high ($\sigma = 1e-3$) and low ($\sigma = 1e-4$) levels and various microstructures.

Parameters	circ-long-het $\sigma_u = 1e^{-4}$	circ-rad-het $\sigma_u = 1e^{-4}$	rad-heli-het $\sigma_u = 1e^{-4}$	circ-long-het $\sigma_u = 1e^{-3}$	circ-rad-het $\sigma_u = 1e^{-3}$	rad-heli-het $\sigma_u = 1e^{-3}$
\hat{e}_a	4.632e-04	4.835e-03	4.466e-03	-1.355e-03	-2.248e-01	-1.418e-01
\hat{e}_b	-1.793e-04	-8.132e-03	-2.026e-03	-4.671e-02	-1.738e-01	-5.960e-02
\hat{e}_{af}	-4.334e-03	-4.031e-02	-1.806e-02	-4.855e-02	-9.203e-01	-6.801e-02
\hat{e}_{bf}	1.847e-03	3.258e-02	1.073e-02	3.515e-02	5.563e-01	5.470e-02
\hat{e}_{a_n}	5.049e-03	-4.218e-02	-7.769e-03	-2.432e-02	1.000e+00	-9.956e-02
\hat{e}_{b_n}	-1.119e-03	9.979e-02	2.589e-04	2.969e-02	9.946e-01	2.204e-02
\hat{e}_{af_s}	1.000e+00	5.264e-01	9.225e-01	1.000e+00	1.000e+00	1.000e+00
\hat{e}_{bf_s}	9.069e-01	-5.964e-01	-3.369e+00	9.118e-01	9.657e-01	9.974e-01
\hat{e}_K	-1.137e-04	4.845e-03	-1.068e-03	7.770e-03	2.997e-01	8.453e-02

Appendix D. Uni-modal deformation mode validation protocols and stress expressions

This appendix summarizes the homogeneous deformation modes used for validation in Section 5.1. We reproduce incompressible biaxial tension and triaxial shear protocols following [10, 11] and evaluate the resulting Cauchy stress responses.

We prescribe a spatially homogeneous deformation gradient

$$\mathbf{F} = \begin{bmatrix} \lambda_f & \gamma_{fs} & \gamma_{fn} \\ \gamma_{sf} & \lambda_s & \gamma_{sn} \\ \gamma_{nf} & \gamma_{ns} & \lambda_n \end{bmatrix}. \quad (\text{D.1})$$

For *biaxial tension*, λ_f and λ_n are prescribed, incompressibility implies $\lambda_s = 1/(\lambda_f \lambda_n)$, and all shear components are set to zero. The hydrostatic pressure is obtained by enforcing $\sigma_{ss} = 0$, which yields the following non-zero stresses

$$\lambda_f \geq 1, \quad \lambda_n \geq 1, \quad \lambda_s = \frac{1}{\lambda_f \lambda_n} \leq 1 : \quad \begin{aligned} \sigma_{ff} &= 2\psi_1 [\lambda_f^2 - \lambda_s^2] + 2\psi_{4ff} \lambda_f^2 \\ \sigma_{nn} &= 2\psi_1 [\lambda_n^2 - \lambda_s^2] + 2\psi_{4nn} \lambda_n^2. \end{aligned} \quad (\text{D.2})$$

Here ψ_\star denotes $\psi_\star = \partial\psi/\partial I_\star$.

For the *triaxial simple shear* cases we consider, $\lambda_f = \lambda_s = \lambda_n \equiv 1$ and a single shear component is activated per test while all others are set to zero. For $\gamma_\star \geq 0$, the non-zero shear stresses read

$$\begin{aligned} \sigma_{sf} &= 2\gamma_{fs}\psi_1 + \psi_{4fs}, & \sigma_{fs} &= 2\gamma_{sf}[\psi_1 + \psi_{4ff}] + \psi_{4fs}, \\ \sigma_{nf} &= 2\gamma_{fn}[\psi_1 + \psi_{4nn}], & \sigma_{fn} &= 2\gamma_{nf}[\psi_1 + \psi_{4ff}], \\ \sigma_{ns} &= 2\gamma_{sn}[\psi_1 + \psi_{4nn}], & \sigma_{sn} &= 2\gamma_{ns}\psi_1. \end{aligned} \quad (\text{D.3})$$

Appendix E. Mixed-modal invariant sampling and admissibility filtering

We sample mixed-modal deformation states by drawing invariants uniformly between the extrema induced by the homogeneous deformation modes in Eq. (D.1). We then reconstruct \mathbf{C} in the local fiber-sheet-normal basis, compute $\sqrt{\mathbf{C}}$ via Schur decomposition, and evaluate the maximum principal Cauchy stress used for admissibility filtering.

We take the minimum and maximum values of the invariants induced by Eq. (D.1) and uniformly sample in between:

$$I_\star \sim \mathcal{U}(I_\star^{\min}, I_\star^{\max}), \quad I_\star \in \{I_1, I_{4ff}, I_{4nn}, I_{4fs}\}. \quad (\text{E.1})$$

where I_\star^{\min} and I_\star^{\max} denote the minimum and maximum deformation invariants seen in the uni-modal biaxial tension and triaxial simple shear experiments studied in Section 5.1. We reconstruct the right Cauchy-Green tensor using the identity $I_1 = I_{4ff} + I_{4ss} + I_{4nn}$ and assuming the same orientation basis as in the uni-modal spatially homogeneous loading case:

$$\begin{aligned} C_{11} &= I_{4ff}, & C_{13} &= C_{31} = C_{23} = C_{32} = 0, \\ C_{22} &= I_1 - I_{4ff} - I_{4nn}, & C_{12} &= C_{21} = I_{4fs}, \\ C_{33} &= I_{4nn}. \end{aligned} \quad (\text{E.2})$$

Using the Schur decomposition [85], we compute the right stretch tensor $\mathbf{U} = \sqrt{\mathbf{C}}$ and use the polar decomposition $\mathbf{F} = \mathbf{R}\mathbf{U}$. We then evaluate the Cauchy stress and extract the maximum principal stress:

$$\sigma_1 = \mathcal{F}_1(\mathbf{J}^{-1}\mathbf{F}\mathbf{S}\mathbf{F}^T) = \mathcal{F}_1(\mathbf{J}^{-1}\mathbf{R}\mathbf{U}\mathbf{S}\mathbf{U}^T) = \mathcal{F}_1(\mathbf{J}^{-1}\mathbf{U}\mathbf{S}\mathbf{U}), \quad (\text{E.3})$$

where $\mathcal{F}_1(\boldsymbol{\sigma}) = \max \text{eig}(\boldsymbol{\sigma})$ and $\mathbf{S} = \partial\Psi/\partial\mathbf{C}$. We accept only physiologically relevant samples satisfying $0.9999 \leq J \leq 1.0001$, aligned with the tissue's assumed quasi-incompressibility, and $\sigma_1 \leq 20.3$ kPa, aligned with the maximum principal stresses measured in experimental protocols on human myocardial tissue [11] (see Table 3 showing peak Cauchy biaxial tensile stresses in the left ventricle). We repeat sampling until 5,000 states are retained.